

# An Integrated Spectrophotometric Survey of Nearby Star-Forming Galaxies

John Moustakas<sup>1</sup> & Robert C. Kennicutt, Jr.<sup>1,2</sup>

## ABSTRACT

We present integrated optical spectrophotometry for a sample of 417 nearby galaxies. Our observations consist of spatially integrated, S/N = 10 – 100 spectroscopy between 3600 and 6900 Å at  $\sim 8$  Å FWHM resolution. In addition, we present nuclear ( $2''.5 \times 2''.5$ ) spectroscopy for 153 of these objects. Our sample targets a diverse range of galaxy types, including starbursts, peculiar galaxies, interacting/merging systems, dusty, infrared-luminous galaxies, and a significant number of normal galaxies. We use population synthesis to model and subtract the stellar continuum underlying the nebular emission lines. This technique results in emission-line measurements reliably corrected for stellar absorption. Here, we present the integrated and nuclear spectra, the nebular emission-line fluxes and equivalent widths, and a comprehensive compilation of ancillary data available in the literature for our sample. In a series of subsequent papers we use these data to study optical star-formation rate indicators, nebular abundance diagnostics, the luminosity-metallicity relation, the dust properties of normal and starburst galaxies, and the star-formation histories of infrared-luminous galaxies.

*Subject headings:* atlases — galaxies: fundamental parameters — galaxies: ISM — galaxies: starburst — galaxies: stellar content — techniques: spectroscopic

## 1. INTRODUCTION

Integrated optical spectrophotometry provides a powerful means of investigating the physical drivers of galaxy evolution. Optical spectral diagnostics may be used to constrain

---

<sup>1</sup>Steward Observatory, University of Arizona, 933 N Cherry Ave., Tucson, AZ 85721, USA; jmoustakas@as.arizona.edu

<sup>2</sup>Current address: Institute of Astronomy, University of Cambridge, Madingley Road, Cambridge CB3 0HA, UK; robk@ast.cam.ac.uk

the star-formation rate, star-formation history, stellar mass, chemical abundance, and dust content of galaxies (e.g., Kauffmann et al. 2003; Panter et al. 2003; Tremonti et al. 2004; Brinchmann et al. 2004). Consequently, tremendous effort has gone into obtaining optical spectroscopy of both nearby and distant galaxies. Kennicutt (1992a, hereafter K92) conducted the first systematic analysis of the integrated spectroscopic properties of 55 nearby galaxies along the Hubble sequence, including a small number of peculiar objects. Optical spectroscopy for the centers of 45 starburst galaxies was presented by Storchi-Bergmann et al. (1995) and McQuade et al. (1995), providing comprehensive spectral coverage from the ultraviolet (Kinney et al. 1993) to the near-infrared (Calzetti 1997a; Wu et al. 2002). Previously, spectroscopic studies of nearby galaxies targeted just their nuclear or high surface-brightness regions, whose physical properties in general are not representative of the whole galaxy. The K92 spectral atlas also provided the first spatially unbiased observations of local galaxies which could be compared directly against observations of distant galaxies. Subsequently, Jansen et al. (2000a,b) presented the Nearby Field Galaxy Survey (NFGS), an integrated spectrophotometric and imaging survey of a representative sample of 196 nearby field galaxies. Gavazzi et al. (2004) have extended the sample of galaxies with integrated spectroscopy to include normal galaxies in higher-density environments, including the Virgo and Coma clusters (see also Gavazzi et al. 2002). However, all these published surveys share a common limitation for high-redshift applications, namely the relatively small representation of starbursts, interacting/merging systems, infrared-luminous galaxies, and other peculiar types that represent only a few percent of the  $z = 0$  population, but which become substantial contributors to the observed high-redshift populations. Consequently, there exists a need for a large integrated spectrophotometric survey that samples a more diverse range of galaxy types.

Large fiber-optic redshift surveys of nearby galaxies are revolutionizing our quantitative understanding of the physical drivers of galaxy evolution. The Sloan Digital Sky Survey (SDSS; York et al. 2000) and the 2dF Galaxy Redshift Survey (2dFGRS; Colless et al. 2001) have obtained optical spectra for nearly  $10^6$  galaxies, providing the opportunity to study the stellar and emission-line properties of nearby galaxies with unprecedented statistical precision. However, these surveys suffer two important limitations for high-redshift applications: incomplete spatial coverage by the spectroscopic aperture, and a magnitude-limited selection criterion that targets primarily the most luminous present-day galaxies. Incomplete spatial coverage, or aperture bias, may be particularly severe since many physical properties of galaxies vary with galactocentric radius (e.g., stellar populations, metallicity, extinction, etc.; see, e.g., Kewley et al. 2005). For example, Tremonti et al. (2004) estimate that aperture bias in the SDSS results in chemical abundance measurements that over-estimate the integrated abundance by at least 25%. Furthermore, these surveys primarily target the most

luminous present-day galaxies, which in general will not be representative of galaxies at an earlier stage in their evolutionary history.

To address these limitations of existing surveys, we have obtained high signal-to-noise ( $S/N = 10 - 100$ ), integrated optical ( $3600 - 6900 \text{ \AA}$ ) spectrophotometry for 417 nearby galaxies. Our survey targets a broad range of galaxy types with ongoing star formation, including ultraviolet- and infrared-luminous starbursts, galaxies with enhanced nuclear or circumnuclear star formation, peculiar galaxies, and interacting/merging systems, and a large number of normal galaxies. Although our sample is incomplete in a strict magnitude-limited sense, the primary objective of our survey was to achieve wide coverage of the physical parameter space spanned by the  $z = 0$  population of star-forming galaxies, focusing on the population of nearby starburst galaxies that likely dominate at high redshift. We utilize the drift-scanning technique developed by K92 to obtain spatially integrated spectroscopy at intermediate ( $\sim 8 \text{ \AA}$  FWHM) spectral resolution. Drift-scanning consists of moving a narrow long-slit back-and-forth across the optical extent of a nearby galaxy that may subtend several arcminutes on the sky. This observational technique results in a luminosity-weighted integrated spectrum analogous to traditional (spatially fixed) spectroscopy of distant galaxies.

In §2 we present our spectroscopic sample. We describe the sample selection, characterize the properties of the sample, describe our observations and data reductions, quantify the spectrophotometric accuracy of the data, and present the final integrated spectral atlas. In §3 we describe `iSPEC1d`, a spectral synthesis and emission-line fitting code we developed to achieve accurate removal of the stellar continuum underlying the nebular emission lines, and in §4 we provide flux and equivalent width measurements of the strong nebular emission lines. Finally, in §5 we summarize our results. To compute distances and absolute magnitudes we adopt a Hubble constant  $H_0 = 70 \text{ km s}^{-1} \text{ Mpc}^{-1}$  (Spergel et al. 2003; Freedman et al. 2001).

## 2. THE DATA

### 2.1. Sample Selection

We draw our sample of galaxies from four primary sources. We select one subset from the First Byurakan Survey of ultraviolet-excess galaxies (Markarian et al. 1989). We primarily target the subsamples studied by Huchra (1977) and Balzano (1983) to weight our selection in favor of starburst galaxies and against active galactic nuclei (AGN). The resulting sample of  $\sim 125$  galaxies contains a diverse collection of galaxy types, including blue compact galaxies

with strong emission lines, starburst nuclei, and normal massive spiral and irregular galaxies with abnormally high SFRs.

An ultraviolet-selected starburst sample such as the one above may be biased toward galaxies with low dust content. Therefore, in order to extend our coverage to dusty starbursts we observe a second subsample of infrared galaxies from the IRAS Warm Galaxy Survey [WGS;  $S_\nu(60 \mu\text{m})/S_\nu(100 \mu\text{m}) > 0.25$ ] and Bright Galaxy Survey (BGS;  $L_{\text{IR}} > 10^{11} L_\odot$ ) (Kim et al. 1995; Veilleux et al. 1995). To extend the baseline in infrared luminosity we include several ultra-luminous infrared galaxies (ULIRGs;  $L_{\text{IR}} > 10^{12} L_\odot$ ; Sanders & Mirabel 1996) from Veilleux et al. (1999). This selection in terms of infrared luminosity and color results in a diverse morphological and spectroscopic sample of  $\sim 100$  galaxies, including relatively normal (but unusually massive) star-forming spirals, edge-on luminous galaxies, AGN-dominated galaxies, and interacting/merging systems.

To increase the sampling of “normal” galaxies and to ensure a more representative range of luminosities, inclinations, and types, we select another subset of galaxies from two volume-limited samples. These observations include  $\sim 75$  galaxies from the 11 HUGS survey (R. C. Kennicutt et al., 2005a, in preparation), an  $\text{H}\alpha$  and ultraviolet imaging survey of galaxies within the 11 Mpc local volume, and 53 star-forming galaxies in the Ursa Major cluster. This nearby cluster ( $d = 19.8$  Mpc; Freedman et al. 2001) is a dynamically young system comprised of many gas-rich spiral galaxies (see Tully et al. 1996, and subsequent papers).

Finally, we incorporate into our sample unpublished integrated spectrophotometry for 35 morphologically disturbed galaxies/systems from the Ph. D. thesis by Anne Turner (Turner 1998). These objects are selected from the Arp (1966) atlas of peculiar galaxies based on visual evidence of recent interactions or merging in the form of tidal tails, bridges, or shells. These data have been obtained using the same instrumental setup and observing technique as the main survey, and have been re-reduced to ensure consistency with our new observations (see §2.4).

In addition to the integrated spectrophotometric observations, during the course of our survey we also obtained nuclear ( $2''.5 \times 2''.5$ ) spectroscopy for  $\sim 30\%$  of the sample. The list of objects with both nuclear and integrated spectra are a heterogenous subset since the nuclear spectra were not the focus of the primary survey. However, we present these data in this paper because they may be useful for a variety of astrophysical applications, such as investigating the connection between the global versus the nuclear/circumnuclear properties of nearby galaxies.

## 2.2. Sample Properties

To increase the archival value of our new spectroscopic observations, we compile multi-wavelength broadband photometry and other relevant galaxy properties using the Nasa Extragalactic Database (NED<sup>3</sup>), the Lyon-Meudon Extragalactic Database (LEDA<sup>4</sup>), and the SIMBAD Astronomical Database<sup>5</sup>. Table 1 presents these global properties in the following thirteen columns, which we describe in more detail below: (1) unique object identification number; (2) galaxy name; (3) other common galaxy name or names; (4) right ascension; (5) declination; (6) heliocentric velocity; (7) foreground Galactic reddening (Schlegel et al. 1998); (8) morphological type; (9) major axis diameter at the 25 mag arcsec<sup>-2</sup> isophote; (10) minor axis diameter at the same isophotal diameter; (11) galaxy position angle; (12) distance; and (13) distance reference.

We adopt coordinates and heliocentric redshifts for our sample from NED, SIMBAD, or LEDA, as noted in Table 1. We obtain major- and minor-axis diameters from the Third Reference Catalog of Bright Galaxies (de Vaucouleurs et al. 1991, hereafter RC3), supplemented with additional measurements from LEDA, the ESO/Uppsala Survey of the ESO(B) Atlas (Lauberts 1982), the Uppsala General Catalog of Galaxies (UGC; Nilson 1973), the Morphological Catalogue of Galaxies (MCG; Vorontsov-Vel’Yaminov & Arkhipova 1962), and the NED “Basic Data,” listed in order of preference. We obtain position angles from the same set of references, supplemented by measurements from either the 2MASS Large Galaxy Atlas (LGA; Jarrett et al. 2003), or the 2MASS Extended Source Catalog (XSC; Jarrett et al. 2000), in that order. We adopt morphological types from the RC3, LEDA, or from our own classification if no other type is available.

Due to the proximity of our sample ( $\sim 1/4$  of our galaxies are nearer than the Virgo cluster), peculiar velocities can be a significant perturbation on the observed radial velocity. Therefore, we search the literature for direct distance estimates to as many galaxies as possible. These distances are based on a variety of techniques, although we give particular preference to the Cepheid period-luminosity relation and the magnitude of the tip of the red-giant branch. Our direct distances rely predominantly on the large compilations by Freedman et al. (2001), Karachentsev et al. (2004), Tonry et al. (2001), and Shapley et al. (2001), listed in order of preference. We use the Cepheid-based distances in Freedman et al. (2001) corrected for metallicity (see also Sakai et al. 2004). We assign members of the Ursa

---

<sup>3</sup><http://nedwww.ipac.caltech.edu>

<sup>4</sup><http://leda.univ-lyon1.fr>

<sup>5</sup><http://simbad.u-strasbg.fr/Simbad>

Major cluster (as defined by Tully et al. 1996) a common distance of  $19.8 \pm 1.6$  Mpc, based on the revised Cepheid distance scale (Freedman et al. 2001). Finally, we compute distances to all other galaxies using the multi-attractor infall model developed by Mould et al. (2000). This model accounts for linear infall onto the Virgo cluster, the Great Attractor, and the Shapley concentration, which we assume to be independent perturbations on the measured radial velocity of the galaxy. For our calculations we adopt the model parameters listed in Table A1 and the set of assumptions enumerated in §2 of Mould et al. (2000). In particular, galaxies that lie within the cone-of-influence of each attractor are forced to the velocity of the attractor (in the Local Group frame-of-reference). We find good statistical agreement between the distances using this model and the direct distances. We also inter-compare distances based the Mould et al. (2000) infall model to the distances in Tully (1988) and again find good statistical agreement and no gross systematic differences.

We compile optical and infrared photometry for our sample using NED’s batch photometry retrieval system. We tabulate total broadband  $UBV$  magnitudes, uncorrected for Galactic extinction and inclination effects, predominantly from the RC3, adopting the RC3  $m_B$  measurements if  $B_T$  magnitudes are unavailable. For objects without RC3 photometry we use LEDA  $UBV$  magnitudes (Prugniel & Heraudeau 1998). We take total J- ( $1.2 \mu\text{m}$ ), H- ( $1.6 \mu\text{m}$ ), and  $K_s$ -band ( $2.2 \mu\text{m}$ ) magnitudes from the 2MASS/LGA (Jarrett et al. 2003) or the 2MASS/XSC (Jarrett et al. 2000), in that order. The 2MASS total magnitudes are derived by extrapolating the observed J-band surface brightness profile to  $\sim 4$  disk scale lengths and integrating in each band (Jarrett et al. 2000). Finally, we tabulate infrared fluxes at 12, 25, 60, and  $100 \mu\text{m}$  for our sample. We obtain these measurements from the IRAS large optical galaxy catalog (Rice et al. 1988), the Bright Galaxy Survey (Soifer et al. 1989), or the Faint Source Catalog (Moshir et al. 1990), ranked in order of preference (following Bell 2003). We correct our  $UBVJHK_s$  magnitudes for foreground Galactic extinction using the  $E(B-V)$  value listed in Table 1 and the O’Donnell (1994) Milky Way extinction curve assuming  $R_V \equiv A_V/E(B-V) = 3.1$ . Table 2 lists these photometric data for our sample.

Figure 1 illustrates the broad range of physical properties spanned by our galaxy sample. In panels (a), (b), (c), and (d), respectively, we plot the distribution of  $B$ -band luminosity,  $B-V$  color, far-infrared (FIR) to  $B$ -band luminosity ratio, and equivalent width (EW) of  $H\alpha$  (*solid-line*, open histogram). For comparison, we show the distributions of the same properties for two other widely used integrated spectrophotometric surveys, the K92 spectral atlas (*dotted-line*, dark grey histogram; Kennicutt 1992a,b) and the NFGS (*dashed-line*, light grey histogram; Jansen et al. 2000a,b). The optical and infrared photometry for all three samples have been collected from the literature in the same way, as described in detail above. Unfortunately,  $V$ -band photometry is only available for 20% of the NFGS; therefore,

we do not plot its  $B-V$  color distribution in Figure 1*b*. We compute the FIR luminosity,  $L(\text{FIR}) \equiv L(40 - 120 \mu\text{m})$ , using the 60 and 100  $\mu\text{m}$  IRAS fluxes according the formula in Helou et al. (1988). The  $\text{H}\alpha$  EWs for our sample (see §4; Table 6) and the NFGS (Jansen et al. 2000a) have been corrected for underlying stellar absorption, but no corrections have been applied to the K92 data. In addition, for the K92 measurements, we follow Kennicutt (1992b) and adopt a constant  $[\text{N II}]/\text{H}\alpha = 0.5$  ratio to convert from  $\text{EW}(\text{H}\alpha + [\text{N II}])$  to  $\text{EW}(\text{H}\alpha)$ .

Figure 1*a* shows that our galaxy sample spans a wide range of blue luminosity, which ensures broad coverage of physical quantities that correlate with luminosity, such as metallicity, excitation, and dust content. Compared to the NFGS, a representative survey of nearby galaxies, our sample includes many more luminous ( $M_B \lesssim -18$  mag) galaxies, in addition to a relatively large percentage of faint ( $M_B > -16$  mag) dwarf galaxies (8% of our sample, compared to 0.8% in the NFGS). The K92 atlas includes predominantly luminous galaxies, as discussed by Jansen et al. (2001). The observed  $B-V$  color distribution of our sample (Fig. 1*b*) varies by one magnitude, indicating a broad range of star-formation histories, from blue, actively star-forming galaxies, to more quiescent (or very dusty) galaxies with red  $B-V$  colors. The range in color is similar to the K92 atlas, although our selection of ultraviolet-excess galaxies (see §2.1) incorporates many more galaxies bluer than  $B-V \simeq 0.3$  mag. Figure 1*c* plots the  $L(\text{FIR})/L(B)$  distribution for the three samples. This ratio characterizes the relative amount of energy absorbed by dust and re-emitted into the infrared. Because we include a large number of infrared-luminous galaxies,  $L(\text{FIR})/L(B)$  in our sample varies by more than a factor of  $\sim 3500$  with a median ratio of 0.07 dex. By comparison, the  $L(\text{FIR})/L(B)$  distributions of the optically selected K92 and NFGS samples are narrower and do not include as many extremely dusty galaxies [ $L(\text{FIR})/L(B) > 10$ ]. Finally, Figure 1*d* compares the  $\text{EW}(\text{H}\alpha)$  distributions of the three samples. The  $\text{EW}(\text{H}\alpha)$  is proportional to the birthrate parameter, or the ratio of the current to the past-average star-formation rate (Kennicutt et al. 1994). Nearly 30% of our galaxies have  $\text{EW}(\text{H}\alpha) > 50 \text{ \AA}$ , compared to 10% in the NFGS, and 40% in the K92 survey.

### 2.3. Observations

We obtain our spectrophotometric observations at the 2.3-meter Bok telescope on Kitt Peak using the Boller & Chivens (B&C) spectrograph. The B&C spectrograph is equipped with a Loral  $1200 \times 800$  square-pixel back-illuminated CCD with  $15 \mu\text{m}$  pixels. The 400 line  $\text{mm}^{-1}$  reflection grating, blazed at  $\sim 5200 \text{ \AA}$ , affords nearly one octave of spectral coverage between 3600 and  $\sim 6900 \text{ \AA}$  with  $2.75 \text{ \AA}$  pixels at a full width at half-maximum (FWHM) resolu-

tion of  $\sim 8 \text{ \AA}$  through a  $2''.5$  slit. The physical scale at the detector, binned by 2 pixels, is  $1''.66 \text{ pixel}^{-1}$ . The usable slit length is  $\sim 3'.3$ , enabling adequate sky subtraction in all but the largest galaxies in our sample. An UV-36 blue-blocking filter eliminates contamination from second-order light; the transmittance through the UV-36 filter is 50% at  $3600 \text{ \AA}$  and 90% at  $4000 \text{ \AA}$ . All the spectra presented in this atlas have been obtained using the identical instrumental setup and observing technique, which ensures data uniformity.

The calibration data for each night include bias frames, dome flats, and evening twilight sky flats. Helium-argon (HeAr) comparison lamps taken during the course of the night at a variety of positions on the sky facilitate wavelength calibration. We observe spectrophotometric standard stars from the CALSPEC<sup>6</sup> (Bohlin et al. 2001) and Massey et al. (1988) star lists at low airmass ( $< 1.2$ ) and near the parallactic angle 4 – 8 times during the night using both  $2''.5$  and  $4''.5$  slits. We observe more than  $\sim 75\%$  of our integrated spectra and  $\sim 85\%$  of our nuclear spectra during clear sky conditions. In §2.4 we discuss our flux-calibration procedure and quantify the relative and absolute spectrophotometric accuracy of our observations.

We implement the drift-scanning technique developed by K92 to obtain integrated spectrophotometry of our sample at the spectral resolution afforded by a  $2''.5$  long-slit (see also Jansen et al. 2000b; Gavazzi et al. 2004). Using this method we scan perpendicular to the slit 10 – 20 times over the optical extent of the galaxy during a single exposure using dedicated telescope control software. By scanning the galaxy multiple times we average over any short-term variations in atmospheric transparency. The choice of scan length and exposure time vary with the size and surface brightness of each object. Our scan lengths range from  $15'' - 800''$  and total exposure times vary from 15 – 120 minutes split into two or more consecutive exposures to facilitate cosmic-ray rejection (see §2.4). The effective time  $t_{\text{eff}}$  spent on a fixed spatial location of the galaxy is given by

$$t_{\text{eff}} = t \left( \frac{2''.5}{\Delta_{\text{scan}}} \right), \quad (1)$$

where  $t$  is the total exposure time and  $\Delta_{\text{scan}}$  is the diameter of the drift-scan perpendicular to the slit in arcseconds. Drift-scanning affords two specific advantages over pointed long-slit spectroscopy. First, it is insensitive to the effects of atmospheric refraction because in general  $\Delta_{\text{scan}} \gg \Delta(\theta)$ , where  $\Delta(\theta)$  is the amount of wavelength-dependent atmospheric refraction in arcseconds as a function of the parallactic angle,  $\theta$  (Filippenko 1982). And second, drift-scanned spectroscopy recovers any light lost due to wavelength-dependent variations in seeing

---

<sup>6</sup><http://www.stsci.edu/instruments/observatory/cdbs/calspec.html>

because, once again,  $\Delta_{\text{scan}} \gg \Delta_{\text{seeing}}$ , where  $\Delta_{\text{seeing}}$  is the FWHM of the seeing disk in arcseconds as a function of wavelength.

In addition to our integrated spectra we have obtained nuclear spectroscopy for  $\sim 30\%$  of our sample. These observations are typically based on 1 – 2 five-minute exposures using a fixed  $2''.5 \times 2''.5$  entrance aperture. For our nuclear spectra we always rotate the slit along the parallactic angle to minimize atmospheric refraction effects (Filippenko 1982). Although many of these nuclear spectra have been obtained during clear or mostly clear observing conditions, we cannot guarantee their absolute spectrophotometric accuracy due to variations in seeing, pointing accuracy, and transparency.

Table 3 presents a summary of our integrated spectrophotometric observations in the following ten columns: (1) galaxy identification number from Table 1; (2) galaxy name; (3) diameter of the drift scan perpendicular to the slit; (4) extraction aperture diameter along the slit; (5) slit position angle; (6) total exposure time; (7) flag indicating whether the spectrum was obtained during clear or non-photometric conditions; (8) uncertainty in the absolute spectrophotometric accuracy of the spectrum (see §2.5); and (9) remarks regarding the individual galaxy or spectral extraction.

## 2.4. Reductions

We reduce our spectroscopic observations using `iSPEC2d`, a generalized long-slit data reduction and analysis software package written in IDL. `iSPEC2d` offers several advantages over some existing spectroscopic data reduction packages such as error propagation, bad pixel tracking, automated wavelength calibration, two-dimensional sky subtraction, minimal pixel resampling (interpolation), and web-page visualizations to facilitate inspection of each step in the reduction procedure.

First we repair dead pixels and bad columns, subtract the overscan noise, trim, subtract the bias frame, and divide by the master flat field. We construct the flat field in the spectral dimension by fitting an high-order cubic spline to a median-averaged dome flat. We average several twilight sky flats and model the residual illumination pattern with a low-order polynomial. We find that flat-fielded exposures of the evening sky are spatially constant at the 1 – 2% level. For each observation we process a corresponding two-dimensional error map, which we construct using the known read-noise and gain of the detector and assuming Poisson statistics.

We measure the two-dimensional mapping between pixels and wavelength using our HeAr lamps. The wavelength residuals are typically 0.2 – 0.4 Å based on 20 – 50 arc lines.

Next, before coadding, we compare the spatial profiles of sequential science exposures to solve for any small shifts (typically  $< 2$  pixels) that may arise from back-lash at the turn-around points of the drift-scan. We remove residual cosmic rays using L. A. COSMIC (van Dokkum 2001), which identifies hot pixels by convolving the data with a Laplacian edge-detection kernel. We experimented with a variety of cosmic-ray rejection schemes and found L. A. COSMIC to be the most reliable. Finally, we examine our cosmic-ray rejected images to verify that neither narrow emission lines nor bright sky lines are inadvertently affected.

Next, we interactively define sky apertures for each object and sky-subtract using the corresponding two-dimensional wavelength map. We fit the over-sampled sky spectrum with an high-order cubic b-spline in the spectral dimension and a first- or second-order polynomial in the spatial dimension, selecting  $2.75 \text{ \AA}$  as the spacing between adjacent b-spline knots. Kelson (2003) discuss in detail the advantages of two-dimensional sky subtraction. We estimate the sky-subtraction uncertainty by computing the error in the mean sky level at each column (wavelength), and propagate this uncertainty into the corresponding error map. We test our simplified assumption of using the error in the mean sky value as the sky-subtraction uncertainty by sky-subtracting 500 Monte Carlo realizations of several hundred galaxy and standard-star spectra spanning a range of sky apertures and exposure times. For each object we measure the standard deviation of the two-dimensional sky model at each column and compare it to our “simple” uncertainty estimate. On average, we find the ratio of the two noise estimates to be unity.

We flux-calibrate our observations using standard stars from an entire run, ranging from 1 – 6 consecutive nights. We obtain the mean sensitivity function for each run by fitting an high-order b-spline fit to 5 – 40 standard stars observed during clear sky conditions and good seeing. We adopt the CALSPEC absolute spectral energy distributions (Bohlin et al. 2001), binned in  $10 \text{ \AA}$  bandpasses, or the Massey et al. (1988) spectrophotometry binned every  $50 \text{ \AA}$  if no CALSPEC calibration is available. We use the nominal Kitt Peak extinction curve to correct for atmospheric extinction and reddening as a function of airmass. In §2.5 we describe our flux calibration procedure in more detail and quantify the relative and absolute spectrophotometric accuracy of our data.

We extract one-dimensional spectra using interactively defined apertures enclosing the full spatial profile of the galaxy, or a fixed  $2''.5$  aperture for our nuclear spectra. We account for the small ( $< 1\%$ ) spatial tilt in our data by fitting a linear function to the flux-weighted trace of the galaxy profile. We carefully treat interacting/merging systems with overlapping spatial profiles by extracting spectra for each individual object and for the composite system. We either exclude contaminating foreground stars from the extraction aperture if they are near the edge of the galaxy, or subtract them from the two-dimensional spectrum using the

following two-step procedure. First, we fit a Gaussian function to the spatial profile of the star averaged every  $\sim 100$  columns to measure the mean variation in FWHM and center. We use low-order polynomial interpolation to estimate these quantities at every column. Next, measure the star’s spectral energy distribution by fitting a Gaussian profile to the stellar profile at every column by constraining the width and center and solving for the amplitude. This procedure yields a robust two-dimensional model of the contaminating star, which we then subtract from the data before extracting the galaxy spectrum normally. We apply a small correction (typically  $\sim 0.5 \text{ \AA}$ ) to each object’s wavelength solution using 10 – 20 night sky lines, and repair sky-subtraction residuals near [O I]  $\lambda 5577$ , Na D  $\lambda 5889$ , [O I]  $\lambda 6300$ , and [O I]  $\lambda 6336$  for display purposes. However, we do not repair sky-subtraction residuals that fall near the Na D interstellar absorption line or the [O I]  $\lambda 6300$  nebular emission line in the lowest-redshift galaxies in our sample. Finally, we correct each spectrum for Galactic reddening and extinction using the Schlegel et al. (1998) dust maps and the O’Donnell (1994) Milky Way extinction curve assuming  $R_V = 3.1$ . The mean (median) reddening for the full sample is  $0.05 \pm 0.07 \text{ mag}$  ( $0.03 \text{ mag}$ ), with  $< 2\%$  of our sample suffering more than  $0.2 \text{ mag}$  of foreground Galactic extinction.

## 2.5. Spectrophotometric Accuracy

In this section we discuss the relative and absolute spectrophotometric accuracy of our observations. Variations in seeing, atmospheric transparency, and pointing prevent the nuclear spectra from being tied to an absolute spectrophotometric scale. However, because our integrated spectra enclose all, or nearly all the optical light of the galaxy, observations made during photometric conditions may be fluxed on an absolute spectrophotometric scale. Drift-scanned long-slit spectroscopy, therefore, is analogous to large-aperture rectangular photometry with the added bonus of yielding spectral information. Note that we do not correct our integrated spectra for any light missed by the drift scan.

We flux-calibrate our spectra using standard stars observed with the  $4''5$  slit during good seeing and clear skies. Assuming comparable seeing for all the standard-star observations, the scatter in the observed sensitivity function relative to the mean quantifies the variation in atmospheric transparency during the course of the observing run. The mean (median) scatter in our sensitivity functions near  $\sim 5500 \text{ \AA}$  is  $0.07^{+0.07}_{-0.05} \text{ mag}$  ( $0.06 \text{ mag}$ ). Unfortunately, even with the  $4''5$  slit we still miss some of the light of the standards. To quantify this effect, we conduct  $20''$  drift scans of several standard stars during photometric conditions in addition to the nominal  $4''5$  slit observations. Figure 2 compares the sensitivity difference between the drift-scanned and  $4''5$  slit observations near  $\sim 5500 \text{ \AA}$ , illustrating that  $0.11 \pm 0.02 \text{ mag}$

of light is lost through the  $4''.5$  slit. We attribute this  $\sim 10\%$  light-loss to seeing: assuming a Gaussian point-spread function, a  $4''.5$ -wide slit encloses just  $\sim 90\%$  of the energy in the median seeing of our observations,  $1''.4$  (FWHM). We add this scalar zero-point shift to every sensitivity function before flux-calibrating, and propagate the 0.02 mag error in the correction into our absolute spectrophotometric error budget. Finally, we also include a 2% uncertainty in the absolute standard-star calibrations (Bohlin et al. 2001). We give the final absolute spectrophotometric uncertainty of each integrated spectrum, excluding systematic uncertainties arising from missing light or systematic sky-subtraction errors, in column (9) of Table 3.

We conduct both internal and external comparisons to further assess the spectrophotometric quality of our observations. First, we compare multiple observations of the same galaxy. Twenty-three objects in our integrated galaxy sample have been observed two or more times and extracted using identical, or nearly identical rectangular apertures. We find that the  $1\sigma$  relative error is  $\pm 3.3\%$  with no wavelength dependence.

Next, we intercompare 11 galaxies in common with the NFGS, both corrected using the same Galactic reddening value. We normalize each pair of spectra to the mean flux around  $5500 \pm 50 \text{ \AA}$  and compute their ratio in  $200 \text{ \AA}$ -wide bins to characterize the variation in continuum shape. We show this comparison in Figure 3 with the NFGS spectrum offset upwards by one unit for clarity. The correspondence between our observations and the NFGS is very good, bearing in mind that in general they are based on different drift-scan lengths, slit position angles, and extraction apertures. Excluding two objects, NGC 3104 and UGC 09560, we find an average relative error of  $\pm 3.7\%$ , with a weak wavelength dependence in the sense that our spectra are bluer than the NFGS by  $\pm 3\%$  between  $4000 \text{ \AA}$  and  $6500 \text{ \AA}$ . Table ?? compares our emission-line equivalent width measurements of [O II]  $\lambda 3727$ , [O III]  $\lambda 5007$ , H $\beta$   $\lambda 4861$ , and H $\alpha$   $\lambda 6563$  for these 11 objects (described in detail in §3) against the Jansen et al. (2000b) measurements. The spectral differences for NGC 3104 may be due to a bright foreground star, which has been subtracted from our data but may not have been subtracted from the NFGS spectrum. For UGC 09560 aperture mismatch may be responsible for the observed discrepancy. Our spectroscopic aperture misses  $\sim 10\%$  of the light while the NFGS aperture encloses the whole galaxy. Alternatively, the NFGS spectrum of UGC 09560 may be suffering from second-order contamination since a blue-blocking filter was not used for the NFGS observations (Jansen et al. 2000b). Despite these discrepancies, however, we conclude that, on average, our observations agree very well with the NFGS.

Another test of our relative and absolute spectrophotometry compares magnitudes synthesized directly from our spectra against published broadband photometry (see §2.1 and Table 2). We synthesize spectrophotometric  $B$ - and  $V$ -band magnitudes using the Bessell

(1990) filter response function and the Lejeune et al. (1997) theoretical spectrum of Vega tied to the Hayes (1985) V-band Vega zero-point. In Figure 4 we plot our synthesized  $B-V$  colors against measurements from the literature. We identify one significant outlier in this comparison, Mrk 0475, a nearby irregular starburst galaxy. The measurements from the literature indicate that the  $B-V$  color for Mrk 0475 is  $\sim 1$  mag, which is unrealistically red for this type of object. The  $1\sigma$  residual scatter including all the points is 0.11 mag, or 0.06 mag if we exclude fourteen  $3\sigma$  outliers, with no systematic offset. Given the typical measurement uncertainty in the photometry from the literature,  $\sim 0.2$  mag, we conclude that our  $B-V$  colors are statistically consistent with the published  $B-V$  colors.

Figure 5 compares published  $B$ - and  $V$ -band magnitudes against our synthesized photometry. Several caveats should be kept in mind for this comparison. First, the photometry from the literature has been taken from the RC3 and LEDA (§2.2), which give total magnitudes extrapolated to infinity, whereas our synthesized magnitudes typically only include the galaxy light within the 25 mag arcsec $^{-2}$  isophote. Unfortunately, these catalogs do not publish the aperture correction used to transform from isophotal to total magnitude, which prevents us from making a more direct comparison. Second, the fraction of light enclosed by our spectroscopic aperture is generally  $< 100\%$ , in particular for the largest galaxies in our sample. Therefore, we anticipate that our synthesized photometry will be systematically fainter than the measurements from the literature, with a possible residual systematic that correlates with galaxy size.

In Figure 5 (*left*) we compare the apparent  $B$  magnitudes,  $m_B$ . The photometric observations exhibit a 0.39 mag residual scatter, or 0.32 mag excluding eight  $3\sigma$  outliers. Not surprisingly, the scatter in our non-photometric observations is much larger, 0.54 mag, or a factor of  $\sim 3.5$ . Below this comparison we plot the magnitude residuals versus  $D_{25}$ , the 25 mag arcsec $^{-2}$  isophotal diameter of the major axis. We find the residuals correlated with  $D_{25}$  in the sense that our synthesized magnitudes miss a larger fraction of the optical light with increasing galaxy size. The median residual increases from 0.0–0.1 dex for the smallest objects in our sample ( $D_{25} \lesssim 0'.5$ ), to 0.3–0.4 dex for objects larger than  $\sim 4'.5$ . In Figure 5 (*right*) we compare our V-band apparent magnitudes against measurements from the literature. The  $1\sigma$  V-band residuals for objects observed during clear conditions is 0.35 mag, or 0.23 mag after clipping seven significant outliers. Galaxies observed during cloudy conditions exhibit a scatter of 0.39 mag excluding one extreme outlier. We also find the median V-band residuals correlated with galaxy size, increasing by a factor of two from the smallest to the largest galaxies in our sample. In conclusion, given all the uncertainties, we find good overall agreement between our synthesized magnitudes and the published broadband photometry. Without isophotal magnitudes for the galaxies in our sample, however, it is very difficult to estimate the light fraction enclosed by our spectroscopic aperture, or to test externally our

absolute spectrophotometric calibration.

Finally, we compare our integrated spectrophotometric  $\text{H}\alpha + [\text{N II}] \lambda\lambda 6548, 6584$  emission-line flux and equivalent-width measurements against published values compiled and homogenized from the literature (R. C. Kennicutt et al., 2005b, in preparation). As described in detail in §3, we carefully subtract the stellar continuum from our spectra using population synthesis before measuring the nebular emission lines; consequently, we account for underlying stellar absorption in our  $\text{H}\alpha$  measurements. The data from the literature are based on narrow-band imaging supplemented with photoelectric measurements, and have been corrected for underlying stellar absorption but not for foreground Galactic reddening. Using a  $15''$  search radius we find 252 overlapping galaxies with  $\text{H}\alpha$  and  $[\text{N II}]$  fluxes detected at more than  $3\sigma$  in both samples, and 206 objects with well-measured equivalent widths. In Figure 6 we compare our emission-line fluxes against data from the literature, coding points according to whether they have been observed during photometric or non-photometric conditions. Overall, we find excellent agreement among the two measurements. Only considering galaxies observed during photometric conditions and removing twelve  $3\sigma$  outliers, we find a  $1\sigma$  residual scatter of 0.12 dex, or 32%, and a median (mean) systematic offset of just 0.02 dex (0.01 dex). In Figure 7 we compare our  $\text{H}\alpha + [\text{N II}] \lambda\lambda 6548, 6584$  equivalent width measurements against the corresponding measurements from the literature, both corrected for stellar absorption. After removing nine significant outliers, we find a median (mean) systematic difference of 0.03 dex (0.04 dex) and a residual scatter of 0.12 dex, or  $\sim 32\%$ .

To summarize, based on a variety of comparisons we find that the spectrophotometric quality of our observations is on average very good. From both internal and external comparisons, we find that our relative spectrophotometric uncertainty is 3 – 4% between  $\sim 3600 \text{ \AA}$  and  $\sim 6900 \text{ \AA}$ . The absolute spectrophotometric accuracy of our data is more difficult to estimate due to the absence of matched-aperture broadband photometry. Nevertheless, neglecting light missed by our extraction apertures, the systematic uncertainty in our absolute spectrophotometry is of order 10 – 30%, and potentially much larger on a case-by-case basis. Because of our inability to estimate this systematic uncertainty accurately, it has not been included in column (9) of Table 3. However, the absence of a systematic offset between our spectrophotometric  $\text{H}\alpha + [\text{N II}] \lambda\lambda 6548, 6584$  fluxes and measurements based on narrow-band imaging indicates that, on average, our observations include all the star-forming regions in our sample of galaxies.

## 2.6. Presentation of the Atlas

In Figure Set 8 we present our integrated spectrophotometric atlas. We plot each spectrum as normalized  $f_\lambda(\lambda)$  versus rest wavelength in Angstroms. We choose the normalization factor for each object to achieve a balance between showing the full range in flux and illustrating the finer details of the continuum. Adjacent to each spectrum we provide a visualization of the galaxy using a logarithmically scaled Digitized Sky Survey image. Each image shows our rectangular spectroscopic aperture as a *solid* line and the 25 mag arcsec<sup>-2</sup> isophotal size of the galaxy from Table 1, where available, as a *dashed* ellipse. The horizontal solid line in the lower-left corner of each image represents 30".

## 3. CONTINUUM & EMISSION-LINE FITTING

### 3.1. Motivation

Typically the integrated spectrum of a galaxy in the optical is a luminosity-weighted sum of an emission-line spectrum superposed on a stellar continuum/absorption-line spectrum. To first order, therefore, we can use population synthesis to model the stellar continuum and subtract it from the data to isolate the nebular emission-line spectrum. This technique, including a simple prescription for dust reddening, offers a powerful way to study the integrated spectral properties of galaxies.

Mathematically, spectral synthesis fitting is a bounded (non-negative) least squares problem. The objective is to find the linear combination of stellar continuum models that optimally reproduces the integrated absorption-line spectrum of the galaxy. High-resolution population synthesis models with broad spectral coverage are ideally suited for this application (e.g., Le Borgne et al. 2004; Bruzual & Charlot 2003). In general, however, degeneracies between age, metallicity, and dust reddening, as well as computational difficulties such as finding a local versus the global minimum, complicate the interpretation of the best-fitting absorption-line spectrum. A better constrained objective is to use population synthesis modeling simply as a means of measuring the nebular emission-line fluxes free from the systematic effects of underlying stellar absorption, without attempting to interpret physically the model continuum.

Most studies correct only the Balmer emission lines for stellar absorption, typically assuming a constant 2 Å (e.g., McCall et al. 1985). However, this value and the assumption of a constant correction only apply to spectroscopy of individual H II regions, where young ( $\lesssim 20$  Myr) stellar populations dominate the underlying continuum. Rosa-González et al.

(2002) demonstrate that the [O II]  $\lambda\lambda 3726, 3729$  doublet also suffers from significant stellar absorption in galaxies with strong Balmer breaks, while the other forbidden nebular lines suffer weak metal-line absorption. In general, the Balmer absorption-line equivalent widths in the integrated spectra of star-forming galaxies vary with wavelength according to the particular star-formation history of each object. Furthermore, the total absorption-line equivalent width, which is independent of spectral resolution, is larger than the absorption correction, or the fraction of the total absorption underlying the nebular emission line. Balmer lines measured from lower spectral resolution spectra suffer larger amounts of underlying stellar absorption. To minimize many of these uncertainties, studies frequently restrict their sample to a minimum H $\alpha$  or H $\beta$  emission-line equivalent width, which unfortunately introduces a bias toward galaxies with larger current to past-average star-formation rates (Kennicutt et al. 1994). By comparison, spectral synthesis modeling accurately determines the underlying stellar continuum for each individual galaxy, enabling even low equivalent-width nebular lines to be measured with high precision. In the following sections we present `iSPEC1d`, our implementation of the technique described above. For similar recent implementations of stellar continuum subtraction we refer the reader to the following papers: Reichardt et al. (2001), Panter et al. (2003), Bruzual & Charlot (2003), Tremonti et al. (2004), Brinchmann et al. (2004), Cid Fernandes et al. (2005), and Savaglio et al. (2005).

### 3.2. Choice of Templates

We choose our continuum templates from the Bruzual & Charlot (2003, hereafter BC03) population synthesis models. We select the BC03 models computed using the ‘Padova 1994’ stellar evolutionary tracks (Girardi et al. 1996, and references therein), the STELIB stellar library (Le Borgne et al. 2003), and the Salpeter (1955) initial mass function (IMF) integrated between  $0.1 M_{\odot}$  and  $100 M_{\odot}$ . At each metallicity BC03 provide 221 spectral energy distributions at unevenly spaced ages ranging from 0 Myr to 20 Gyr. The FWHM resolution of the models is  $3 \text{ \AA}$  between  $3200 \text{ \AA}$  and  $9500 \text{ \AA}$  with  $1 \text{ \AA}$  binning.

After extensive experimentation we select eight instantaneous-burst, solar-metallicity models corresponding to the following ages: 0, 5, 25, 102, 255, 641, 1434, and 12000 Myr (Fig. 9). Clearly, there exists a degeneracy between selecting young, solar-metallicity models, versus more evolved metal-poor simple stellar populations. However, we emphasize that the primary motivation for fitting the stellar continuum is to correct quantitatively and self-consistently the Balmer emission lines for stellar absorption, and to enable measurement of weak nebular emission lines. In this context, eight solar-metallicity templates adequately reproduce the stellar continua of our galaxies. Furthermore, our emission-line fluxes do not

change significantly if we select fewer or more templates, or if we allow the stellar metallicity to vary from solar. In a future paper we will investigate the stellar metallicities and detailed star formation histories of the galaxies in our sample using more generalized population synthesis fitting techniques (e.g., Panter et al. 2003; Bruzual & Charlot 2003; Cid Fernandes et al. 2005).

### 3.3. The Fitting Algorithm

We begin with a flux-calibrated galaxy spectrum  $S(\lambda)$  as a function of wavelength  $\lambda$ , a variance spectrum  $\sigma^2(\lambda)$ , and a set of  $N$  single metallicity population synthesis templates  $\mathcal{T}^i(\lambda)$  ( $i = 1, \dots, N$ ). Let  $\xi_S$  be the FWHM resolution of the data due to instrumental and stellar velocity broadening. Because our instrumental resolution,  $\sim 8 \text{ \AA}$  FWHM, or  $\sim 435 \text{ km s}^{-1}$  at  $5500 \text{ \AA}$ , prohibits us from measuring the stellar velocity dispersion  $\sigma_*$  directly, we assume a fixed  $\sigma_* = 100 \text{ km s}^{-1}$  for the whole sample. We obtain only minimal improvement in the quality of the continuum subtraction if we adopt a velocity dispersion that varies with the galaxy luminosity based on, for example, the Tully-Fisher relation. Computationally, our algorithm searches for the optimal non-negative linear combination of  $\mathcal{T}^i(\lambda)$  that best reproduces the observed absorption-line spectrum, subtracts it from the data, and then simultaneously fits all the nebular emission lines using physically motivated constraints on the Gaussian line profiles. We summarize this procedure in more detail next.

1. First, we shift all the observed quantities to the rest-frame using the redshifts in Table 1:  $\lambda = \lambda_{\text{obs}}/(1+z)$ ,  $S = S_{\text{obs}}(1+z)$ ,  $\sigma_S^2 = \sigma_{S_{\text{obs}}}^2(1+z)^2$ , and  $\xi_S = \xi_{S_{\text{obs}}}/(1+z)$ . Consequently, all measured quantities such as equivalent widths are returned in the rest frame-of-reference.
2. Next, we resample the fitting templates onto the rest wavelength spacing and pixel size of the data using high-order spline interpolation. We broaden the templates to the spectral resolution of the data using a Gaussian convolution kernel:

$$\mathcal{T}_B^i(\lambda) = \frac{1}{\sqrt{2\pi}\sigma(\lambda)} \int_{\lambda_{\min}}^{\lambda_{\max}} d\lambda' \mathcal{T}^i(\lambda') \exp\left[-\frac{(\lambda - \lambda')^2}{2\sigma^2(\lambda')}\right], \quad (2)$$

where

$$\sigma(\lambda) \equiv \frac{\sqrt{\xi_S^2(\lambda) - \xi_T^2(\lambda)}}{2\sqrt{2\ln 2}} \quad (3)$$

is the Gaussian broadening function width and  $\xi_T = 3 \text{ \AA}$  is the FWHM resolution of the templates.

3. We mask all pixels within  $\pm 20 \text{ \AA}$  of the nebular emission lines, the Na D  $\lambda\lambda 5890, 5896$  interstellar absorption doublet, and the [O I]  $\lambda 5577$  night sky line, as well as the atmospheric telluric absorption band at  $6850 - 6960 \text{ \AA}$ .
4. The best-fitting model spectrum  $\mathcal{F}(\lambda)$  is given by

$$\mathcal{F}(\lambda) = \sum_{i=1}^N A_i \mathcal{T}_B^i(\lambda) 10^{-0.4 \alpha_i E(B-V) k(\lambda)} \quad (4)$$

where the  $A_i$  are the non-negative coefficients we require,  $k(\lambda)$  is an assumed reddening curve, and the product  $\alpha_i E(B-V)$  controls the reddening of each template (described in §3.4). To find the  $A_i$  coefficients we minimize the  $\chi^2$  statistic using MPFIT<sup>7</sup>, where

$$\chi^2 \equiv \sum_{j=1}^M \frac{[S(\lambda_j) - \mathcal{F}(\lambda_j)]^2}{\sigma^2[S(\lambda_j)]} \quad (5)$$

and  $M$  is the number of unmasked pixels in the continuum.

5. We iterate steps 1 through 4 twice, but after the first iteration we improve on the initial absorption-line redshift of the galaxy by cross-correlating the best-fitting model spectrum  $\mathcal{F}(\lambda)$  with the observed spectrum  $S(\lambda)$ . This step accounts for small errors in the input redshift or wavelength array, although we do not allow the redshift to vary by more than  $\pm 500 \text{ km s}^{-1}$ . In addition, based on some simple simulations, to prevent spurious shifts we demand a median S/N  $> 10$  in the continuum before updating the redshift. On the second iteration we also input the best-fitting coefficients from the previous iteration as an initial guess to ensure rapid convergence.
6. Finally, we subtract the best-fitting absorption-line spectrum from the data to obtain a pure emission-line spectrum,  $\mathcal{E}(\lambda) \equiv S(\lambda) - \mathcal{F}(\lambda)$ . We model  $\mathcal{E}(\lambda)$  as a sum of  $n_{\text{line}}$  Gaussian functions at the rest wavelengths of the nebular emission lines of interest. The velocity width of each emission line is given by  $\sigma_{\text{line}} = \sqrt{\sigma_{\text{gas}}^2 + \sigma_S^2}$ , where  $\sigma_{\text{gas}}$  is the intrinsic velocity dispersion of the gas in  $\text{km s}^{-1}$  and  $\sigma_S = 1.273 \times 10^5 \xi_T / \lambda_{\text{line}}$  is the instrumental resolution in  $\text{km s}^{-1}$  and  $\lambda_{\text{line}}$  is the wavelength of the emission line. We

---

<sup>7</sup>A Levenberg-Marquardt least-squares minimization routine available at <http://cow.physics.wisc.edu/~craigm/idl>.

tie all the Balmer emission lines together by constraining their  $\sigma_{\text{gas}}$  and redshift. We apply the same constraints separately to the forbidden emission lines. This procedure reduces the number of free emission-line parameters from  $3 \times n_{\text{line}}$  to  $n_{\text{line}} + 2$  and succeeds remarkably well at fitting weak emission lines since their profiles are tied to stronger lines.

The final outputs from `iSPEC1d` are the best-fitting absorption-line spectrum and the integrated fluxes of the nebular emission lines, self-consistently corrected for underlying stellar absorption. In Figure 10 we show four examples of our spectral synthesis modeling results. In the left panels we plot the integrated spectrum and the best-fitting stellar continuum for NGC 0034, NGC 4651, NGC 3893, and NGC 0337. For clarity we do not plot the fits to the nebular emission lines. In the right panels we show an expanded view of the data and our model fits centered on the  $\text{H}\beta$  nebular emission line. In all these objects  $\text{H}\beta$  is severely affected by underlying stellar absorption. After continuum subtraction, we measure  $\text{H}\beta$  emission-line EWs of 1.2, 3.7, 5.7, and 10.4 Å, from top to bottom, respectively. The EWs of the absorption corrections are 5.9, 3.9, 4.6, and 5.2 Å, respectively. Frequently, population synthesis cannot be used to model the integrated stellar continua of galaxies, for example, if the spectra have not been flux-calibrated, or if the signal-to-noise ratio is too low. In these cases, a statistical Balmer absorption correction is normally adopted. However, as discussed in §3.1, in general, the appropriate correction varies across the Balmer-line sequence according to the particular star-formation history of each galaxy, and depends on the spectral resolution of the data, being larger for lower-resolution spectra. In our integrated sample the average  $\text{H}\beta$  and  $\text{H}\alpha$  stellar absorption corrections are  $4.4 \pm 0.63$  Å and  $2.8 \pm 0.38$  Å. For comparison, Kobulnicky et al. (1999) find that the  $\text{H}\beta$  absorption correction in their sample and in the K92 atlas ranges from 1 – 6 Å, with a mean of  $3 \pm 2$  Å.

### 3.4. Reddening Model

Virtually all of the galaxies in our sample require continuum reddening to achieve reasonable fits to their integrated or nuclear spectrum. Given our poor understanding of the effects of dust attenuation on the integrated spectral properties of galaxies (e.g., Witt & Gordon 2000), we opt for a simple, physically motivated model. For our sample we adopt the Charlot & Fall (2000) galactic attenuation curve, parameterized as  $k(\lambda) = R_V (\lambda/5500 \text{ \AA})^{-0.7}$ , where  $R_V = 5.9$ . Below, we discuss the effect of selecting a different  $k(\lambda)$ .

Based on some simple arguments we expect the young stellar populations to suffer a larger amount of dust extinction relative to the old stellar populations. Because of their short lifetimes, early-type stars are located near their dusty, natal star-forming regions, whereas

late-type stars are more uniformly dispersed throughout the galaxy where interstellar dust extinction is less severe (Calzetti et al. 1994; Mayya & Prabhu 1996; Charlot & Fall 2000; Zaritsky et al. 2002). To parameterize this observational constraint we define

$$E(B-V)_{\text{old}} \equiv \alpha E(B-V)_{\text{young}}, \quad (6)$$

where  $E(B-V)_{\text{young}}$  and  $E(B-V)_{\text{old}}$  correspond to the attenuation of the stellar populations younger and older than 10 Myr, respectively, and  $0 \leq \alpha \leq 1$  is a constant. The time boundary between young and old stellar populations roughly corresponds to the dispersal time for giant molecular clouds (e.g., Blitz & Shu 1980). Computationally, we solve for the best-fitting parameters  $E(B-V)_{\text{young}}$  and  $\alpha$ , and use equation (6) to obtain  $E(B-V)_{\text{old}}$ . We also tested a one-parameter reddening model, fixing  $\alpha \equiv 1$  for all ages and solving for a scalar reddening value,  $E(B-V)$ .

In general we achieve better continuum fits with our two-parameter reddening model, which is not surprising given the added flexibility. We also find, however, that the optimal reddening parameters are highly degenerate with the best-fitting star-formation history. For example, we obtain comparable  $\chi^2$  values with a highly reddened young stellar population as with an unreddened, evolved stellar population. This effect is well-known as the age-reddening degeneracy. Ultimately, since we are not attempting to constrain the star-formation histories of our sample, only to achieve robust stellar absorption corrections, we adopt the one-parameter reddening model as our default, and post-pone a more in-depth analysis of these degeneracies to a future study.

How physical are the derived continuum reddening values? In Figure 11 we explore this question by plotting the derived continuum reddening,  $E(B-V)$ , versus the nebular reddening as derived from the  $H\alpha/H\beta$  Balmer decrement for our nuclear and integrated spectra. Using a Spearman rank correlation test we find these independent variables correlated at  $> 10\sigma$  significance. For reference we overplot lines of constant  $\alpha = (0.5, 0.25, 0.1)$ , assuming that the nebular reddening traces the obscuration of the young stellar populations. We find that, on average, the stellar continuum suffers a fractional amount of dust extinction relative to the nebular lines. For the integrated spectra the median (mean) ratio is 0.34 ( $0.32 \pm 0.21$ ), and 0.45 ( $0.40 \pm 0.21$ ) for the nuclear spectra. For comparison, based on an analysis of the centers ( $10'' \times 20''$ ) of a sample of  $\sim 40$  starburst galaxies, Calzetti (1997b) find an average ratio of  $0.44 \pm 0.03$  (see also Calzetti et al. 1994; Storchi-Bergmann et al. 1994; Calzetti et al. 2000).

Finally, we explore the effect of choosing a different  $k(\lambda)$  on the quality of the continuum fits and on the derived emission-line fluxes and equivalent widths (see §4). To conduct

this test we refit our integrated spectral atlas with a standard Milky Way extinction curve ( $R_V = 3.1$ ; O’Donnell 1994), and with the Small Magellanic Cloud (SMC) extinction curve ( $R_V = 2.74$ ; Gordon et al. 2003). We compare these results against the values we obtain using our default Charlot & Fall (2000) attenuation curve. We find no significant changes in the quality of the continuum fits using either the Milky Way or SMC extinction curves: the standard deviation of the ratio of the derived  $\chi^2$  values is 1.4% and 1.9%, respectively, with no systematic differences. The residuals of the best-fitting  $E(B-V)$  values exhibit no systematic differences, and a scatter of just  $\pm 3\%$  based on either the Milky Way or SMC extinction curves. Finally, we find no systematic residuals among the emission-line fluxes and equivalent widths measured using any of the three parameterizations of  $k(\lambda)$ . Moreover the standard deviation of the residuals are always  $< 1.5\%$ , which is well within the typical measurement uncertainty of the data.

#### 4. EMISSION-LINE MEASUREMENTS

After continuum subtraction the residual spectrum is a pure emission-line spectrum readily modeled using multi-Gaussian profile fitting. In our integrated and nuclear spectra we simultaneously fit the  $H\alpha$ ,  $H\beta$ ,  $H\gamma$ , and  $H\delta$  Balmer emission lines and the following forbidden nebular emission lines: [O II]  $\lambda\lambda 3726, 3729$ , [O III]  $\lambda\lambda 4959, 5007$ , [O I]  $\lambda 6300$ , [N II]  $\lambda\lambda 6548, 6584$ , and [S II]  $\lambda\lambda 6716, 6731$ . Because the [O II] doublet is unresolved at our spectral resolution we sum the individual Gaussian components to form the [O II]  $\lambda 3727$  emission line. In addition to the velocity width and redshift constraints described in §3.3, we also constrain the [N II] doublet ratio,  $[\text{N II}]\lambda 6584/\lambda 6548 \simeq 3$  (Storey & Zeippen 2000), since these lines are moderately blended with  $H\alpha$  at our spectral resolution. Furthermore, we do not allow the emission-line redshift to differ from the continuum redshift by more than  $\pm 1000 \text{ km s}^{-1}$  and we forbid the intrinsic velocity width from exceeding  $500 \text{ km s}^{-1}$ .

In Tables 4 and 5 we present the emission-line fluxes,  $1\sigma$  flux errors, and  $1\sigma$  upper limits for the strong nebular emission lines in our integrated and nuclear spectra, respectively. These measurements have been corrected for foreground Galactic extinction using the reddening values in Table 1 and the O’Donnell (1994) Milky Way extinction curve, and for underlying stellar absorption as described in §3.3; they have not been corrected for reddening intrinsic to the galaxy. We compute upper limits for undetected ( $S/N < 1$ ) emission lines by measuring the standard deviation of the continuum near the line,  $\delta_{lc}$ , and determining the total (instrumental plus intrinsic) velocity width at that wavelength,  $\sigma_{\text{line}}$ . The intrinsic velocity width can be estimated because the emission lines are tied together. The  $1\sigma$  upper limit is then given by  $\sqrt{2\pi} \sigma_{\text{line}} \delta_{lc}$ , assuming that the undetected line is a Gaussian function

whose sigma-width is  $\sigma_{\text{line}}$  Angstroms.

The errors given in Tables 4 and 5 underestimate the true error because they only incorporate statistical sources of uncertainty due to Poisson noise, read noise, sky subtraction, and sensitivity function division. We conduct two experiments to estimate the systematic uncertainty in our flux measurements. First, we compare the measured [O III]  $\lambda\lambda 4959, 5007$  doublet ratio to the theoretical ratio: [O III]  $\lambda 5007/\lambda 4959 \simeq 3$  (Storey & Zeippen 2000). We find that for  $\text{EW}([\text{O III}] \lambda 4959) \gtrsim 3 \text{ \AA}$  the measured ratio agrees with the theoretical value within  $\pm 4\%$ . In our second test we select the [O III]  $\lambda 5007$  emission line, which is well-isolated and exhibits a wide range of intensities, and compare the Gaussian-integrated flux against the total flux within  $\pm 3 \sigma_{\text{line}}$  of the line center, where  $\sigma_{\text{line}}$  is the total (instrumental plus intrinsic) Gaussian line-width. Once again we derive a mean scatter of  $\pm 4\%$  with no systematic dependence on the emission-line equivalent width. In conclusion we recommend adding a 4% systematic error in quadrature to the uncertainties given in Tables 4 and 5.

The equivalent width measurements and  $1\sigma$  upper limits for the strong nebular lines in our integrated and nuclear spectra, respectively, are given in Tables 6 and 7. In these tables we adopt the convention that emission-line equivalent widths are positive. As discussed above the equivalent widths errors only reflect the statistical uncertainty in the measurement. To determine the equivalent width of a line we divide its flux by the continuum at the line-center, neglecting any small-scale variations in the continuum over the line-profile. We compute the local continuum as the average flux in two bandpasses centered on the rest wavelength of the line,  $\lambda_0$ , given by  $[\lambda_0 + 3 \sigma_{\text{line}}, \lambda_0 + 10 \sigma_{\text{line}}]$  and  $[\lambda_0 - 10 \sigma_{\text{line}}, \lambda_0 - 3 \sigma_{\text{line}}]$ , where  $\sigma_{\text{line}}$  is the total (intrinsic plus instrumental) Gaussian width of the line in Angstroms. This measurement is made on the emission-line subtracted spectrum  $S(\lambda) - \mathcal{E}(\lambda)$  to ensure that nearby emission lines do not bias the local continuum measurement. The equivalent widths of the Balmer emission lines must be treated separately from the forbidden lines due to the strong underlying stellar absorption. For each Balmer line we define red and blue pseudo-continuum bandpasses, given in Table ??, analogous to the Lick indices (Worthey et al. 1994; Worthey & Ottaviani 1997; Trager et al. 1998). Finally, we interpolate the mean continuum flux in the red and blue bandpasses at the line-center and divide by the emission-line flux to derive the equivalent width.

## 5. SUMMARY

We conclude by briefly highlighting a few key aspects of our survey with respect to sample selection, data quality, and analysis methods, and by describing a handful of the scientific investigations we are currently pursuing with these data. The strengths of our

survey are the size (417 galaxies) and diversity of the sample, the signal-to-noise (10 – 100) and relative spectrophotometric accuracy ( $\sim 4\%$ ) of the observations, and the quantitative methods we have developed to measure the nebular emission lines. Our sample includes a wide range of galaxy types, from low-luminosity dwarf starburst galaxies such as I Zw 018 (UGCA 166) and NGC 1569; large disk galaxies such Messier 51a (NGC 5194) and NGC 2903; interacting/merging systems at various stages of their dynamical interaction such as the Mice (NGC 4676) and the Antennae (Arp 244); and luminous- and ultra-luminous infrared galaxies such as Arp 220, to name just a few specific examples. The spectrophotometric observations we present constitute a homogenous data set obtained using the same telescope, instrumental setup, and observing technique, which minimizes or eliminates systematic errors in the data acquisition and data processing. Furthermore, we have reduced the data using a new long-slit data reduction software package (`iSPEC2d`), which enables us to propagate carefully the uncertainties in the data through every stage of the reductions. Finally, we measure the nebular emission lines precisely and free from the systematic effects of stellar absorption using population synthesis modeling and subtraction of the stellar continuum (`iSPEC1d`).

The integrated spectra we have obtained are spatially unbiased, thereby making them ideal for studying the global spectrophotometric properties of nearby galaxies. In addition, our observations may serve as a unique reference sample for interpreting the properties of spatially unresolved, distant galaxies. In a series of subsequent papers we will be using these data to study and calibrate rest-frame optical star-formation rate indicators (Moustakas et al. 2005), emission-line abundance diagnostics, the physical sources of scatter in the luminosity-metallicity relation, the geometry and dust content of normal and starburst galaxies, and the global star-formation histories of infrared-luminous galaxies.

The authors would like to thank Christy Tremonti for contributing invaluable technical expertise during the course of this project, and for constructive comments on an earlier draft of the paper. J. M. would also like to acknowledge discussions, encouragement, and other helpful contributions from Sanae Akiyama, Eric Bell, Daniel Eisenstein, Doug Finkbeiner, Karl Gordon, Joannah Hinz, Janice Lee, Andy Marble, Leonidas Moustakas, Chien Peng, Amy Stutz, and Dennis Zaritsky. The anonymous referee’s suggestions also helped improve the clarity of the paper. The data reduction software developed during the course of this project benefited enormously from IDL routines written by David Schlegel, Scott Burles, Doug Finkbeiner, and Craig Markwardt, and from the IDL Astronomy User’s Library, which is maintained by Wayne Landsman at the Goddard Space Flight Center. Funding for this project has been provided by NSF grant AST-0307386, NASA grant NAG5-8326, and a SINGS grant, provided by NASA through JPL contract 1224769. This research has made use of NASA’s Astrophysics Data System Bibliographic Services, the VizieR catalogue access

tool, the SIMBAD database, operated at CDS, Strasbourg, France, the LEDA database, and the NASA/IPAC Extragalactic Database, which is operated by the Jet Propulsion Laboratory, California Institute of Technology, under contract with the National Aeronautics and Space Administration.

*Facility:* Bok (Boller & Chivens spectrograph)

## REFERENCES

- Arp, H. 1966, Atlas of Peculiar Galaxies (Atlas of Peculiar Galaxies Publisher: California Institute of Technology, Pasadena, CA, 1966)
- Balzano, V. A. 1983, ApJ, 268, 602
- Bell, E. F. 2003, ApJ, 586, 794
- Bessell, M. S. 1990, PASP, 102, 1181
- Blitz, L., & Shu, F. H. 1980, ApJ, 238, 148
- Bohlin, R. C., Dickinson, M. E., & Calzetti, D. 2001, AJ, 122, 2118
- Brinchmann, J., Charlot, S., White, S. D. M., Tremonti, C., Kauffmann, G., Heckman, T., & Brinkmann, J. 2004, MNRAS, 351, 1151
- Bruzual, G., & Charlot, S. 2003, MNRAS, 344, 1000
- Calzetti, D. 1997a, AJ, 113, 162
- Calzetti, D. 1997b, in American Institute of Physics Conference Series, 403–+
- Calzetti, D., Armus, L., Bohlin, R. C., Kinney, A. L., Koornneef, J., & Storchi-Bergmann, T. 2000, ApJ, 533, 682
- Calzetti, D., Kinney, A. L., & Storchi-Bergmann, T. 1994, ApJ, 429, 582
- Charlot, S., & Fall, S. M. 2000, ApJ, 539, 718
- Cid Fernandes, R., Mateus, A., Laerte, S. J., Stasinska, G., & Gomes, J. M. 2005, MNRAS, 358, 363
- Colless, M., Dalton, G., Maddox, S., Sutherland, W., Norberg, P., Cole, S., Bland-Hawthorn, J., Bridges, T., Cannon, R., Collins, C., Couch, W., Cross, N., Deeley, K., De Propris, R., Driver, S. P., Efsthathiou, G., Ellis, R. S., Frenk, C. S., Glazebrook, K., Jackson, C., Lahav, O., Lewis, I., Lumsden, S., Madgwick, D., Peacock, J. A., Peterson, B. A., Price, I., Seaborne, M., & Taylor, K. 2001, MNRAS, 328, 1039
- de Vaucouleurs, G., de Vaucouleurs, A., Corwin, H. G., Buta, R. J., Paturel, G., & Fouque, P. 1991, Third Reference Catalogue of Bright Galaxies (Volume 1-3, XII, 2069 pp. 7 figs.. Springer-Verlag Berlin Heidelberg New York)
- Filippenko, A. V. 1982, PASP, 94, 715

- Freedman, W. L., Madore, B. F., Gibson, B. K., Ferrarese, L., Kelson, D. D., Sakai, S., Mould, J. R., Kennicutt, R. C., Ford, H. C., Graham, J. A., Huchra, J. P., Hughes, S. M. G., Illingworth, G. D., Macri, L. M., & Stetson, P. B. 2001, *ApJ*, 553, 47
- Gavazzi, G., Bonfanti, C., Sanvito, G., Boselli, A., & Scodreggio, M. 2002, *ApJ*, 576, 135
- Gavazzi, G., Zaccardo, A., Sanvito, G., Boselli, A., & Bonfanti, C. 2004, *A&A*, 417, 499
- Girardi, L., Bressan, A., Chiosi, C., Bertelli, G., & Nasi, E. 1996, *A&AS*, 117, 113
- Gordon, K. D., Clayton, G. C., Misselt, K. A., Landolt, A. U., & Wolff, M. J. 2003, *ApJ*, 594, 279
- Hayes, D. S. 1985, in *IAU Symp. 111: Calibration of Fundamental Stellar Quantities*, 225–249
- Helou, G., Khan, I. R., Malek, L., & Boehmer, L. 1988, *ApJS*, 68, 151
- Huchra, J. P. 1977, *ApJS*, 35, 171
- Jansen, R. A., Fabricant, D., Franx, M., & Caldwell, N. 2000a, *ApJS*, 126, 331
- Jansen, R. A., Franx, M., & Fabricant, D. 2001, *ApJ*, 551, 825
- Jansen, R. A., Franx, M., Fabricant, D., & Caldwell, N. 2000b, *ApJS*, 126, 271
- Jarrett, T. H., Chester, T., Cutri, R., Schneider, S., Skrutskie, M., & Huchra, J. P. 2000, *AJ*, 119, 2498
- Jarrett, T. H., Chester, T., Cutri, R., Schneider, S. E., & Huchra, J. P. 2003, *AJ*, 125, 525
- Karachentsev, I. D., Karachentseva, V. E., Huchtmeier, W. K., & Makarov, D. I. 2004, *AJ*, 127, 2031
- Kauffmann, G., Heckman, T. M., White, S. D. M., Charlot, S., Tremonti, C., Brinchmann, J., Bruzual, G., Peng, E. W., et al. 2003, *MNRAS*, 341, 33
- Kelson, D. D. 2003, *PASP*, 115, 688
- Kennicutt, R. C. 1992a, *ApJS*, 79, 255
- . 1992b, *ApJ*, 388, 310
- Kennicutt, R. C., Tamblyn, P., & Congdon, C. E. 1994, *ApJ*, 435, 22

- Kewley, L. J., Jansen, R. A., & Geller, M. J. 2005, *PASP*, 117, 227
- Kim, D.-C., Sanders, D. B., Veilleux, S., Mazzarella, J. M., & Soifer, B. T. 1995, *ApJS*, 98, 129
- Kinney, A. L., Bohlin, R. C., Calzetti, D., Panagia, N., & Wyse, R. F. G. 1993, *ApJS*, 86, 5
- Kobulnicky, H. A., Kennicutt, R. C., & Pizagno, J. L. 1999, *ApJ*, 514, 544
- Lauberts, A. 1982, *ESO/Uppsala survey of the ESO(B) atlas (Garching: European Southern Observatory (ESO), 1982)*
- Le Borgne, D., Rocca-Volmerange, B., Prugniel, P., Lançon, A., Fioc, M., & Soubiran, C. 2004, *A&A*, 425, 881
- Le Borgne, J.-F., Bruzual, G., Pelló, R., Lançon, A., Rocca-Volmerange, B., Sanahuja, B., Schaerer, D., Soubiran, C., & Vílchez-Gómez, R. 2003, *A&A*, 402, 433
- Lejeune, T., Cuisinier, F., & Buser, R. 1997, *A&AS*, 125, 229
- Markarian, B. E., Lipovetsky, V. A., Stepanian, J. A., Erastova, L. K., & Shapovalova, A. I. 1989, *Soobshcheniya Spetsial'noj Astrofizicheskoy Observatorii*, 62, 5
- Massey, P., Strobel, K., Barnes, J. V., & Anderson, E. 1988, *ApJ*, 328, 315
- Mayya, Y. D., & Prabhu, T. P. 1996, *AJ*, 111, 1252
- McCall, M. L., Rybski, P. M., & Shields, G. A. 1985, *ApJS*, 57, 1
- McQuade, K., Calzetti, D., & Kinney, A. L. 1995, *ApJS*, 97, 331
- Moshir, M., Kopan, G., Conrow, T., McCallon, H., Hacking, P., Gregorich, D., Rohrbach, G., Melnyk, M., et al. 1990, *BAAS*, 22, 1325
- Mould, J. R., Huchra, J. P., Freedman, W. L., Kennicutt, R. C., Ferrarese, L., Ford, H. C., Gibson, B. K., Graham, J. A., et al. 2000, *ApJ*, 529, 786
- Moustakas, J., Kennicutt, R. C., & Tremonti, C. 2005, *ApJ*, submitted
- Nilson, P. 1973, *Nova Acta Regiae Soc. Sci. Upsaliensis Ser. V*, 0
- O'Donnell, J. E. 1994, *ApJ*, 422, 158
- Panther, B., Heavens, A. F., & Jimenez, R. 2003, *MNRAS*, 343, 1145

- Prugniel, P., & Heraudeau, P. 1998, *A&AS*, 128, 299
- Reichardt, C., Jimenez, R., & Heavens, A. F. 2001, *MNRAS*, 327, 849
- Rice, W., Lonsdale, C. J., Soifer, B. T., Neugebauer, G., Koplan, E. L., Lloyd, L. A., de Jong, T., & Habing, H. J. 1988, *ApJS*, 68, 91
- Rosa-González, D., Terlevich, E., & Terlevich, R. 2002, *MNRAS*, 332, 283
- Sakai, S., Ferrarese, L., Kennicutt, R. C., & Saha, A. 2004, *ApJ*, 608, 42
- Salpeter, E. E. 1955, *ApJ*, 121, 161
- Sanders, D. B., & Mirabel, I. F. 1996, *ARA&A*, 34, 749
- Savaglio, S., Glazebrook, K., Le Borgne, D., Juneau, S., Abraham, R., Chen, H. ., Crampton, D., McCarthy, P., Carlberg, R., Marzke, R., Roth, K., Jorgensen, I., & Murowinski, R. 2005, *ArXiv Astrophysics e-prints*
- Schlegel, D. J., Finkbeiner, D. P., & Davis, M. 1998, *ApJ*, 500, 525
- Shapley, A., Fabbiano, G., & Eskridge, P. B. 2001, *ApJS*, 137, 139
- Soifer, B. T., Boehmer, L., Neugebauer, G., & Sanders, D. B. 1989, *AJ*, 98, 766
- Spergel, D. N., Verde, L., Peiris, H. V., Komatsu, E., Nolta, M. R., Bennett, C. L., Halpern, M., Hinshaw, G., Jarosik, N., Kogut, A., Limon, M., Meyer, S. S., Page, L., Tucker, G. S., Weiland, J. L., Wollack, E., & Wright, E. L. 2003, *ApJS*, 148, 175
- Storchi-Bergmann, T., Calzetti, D., & Kinney, A. L. 1994, *ApJ*, 429, 572
- Storchi-Bergmann, T., Kinney, A. L., & Challis, P. 1995, *ApJS*, 98, 103
- Storey, P. J., & Zeppen, C. J. 2000, *MNRAS*, 312, 813
- Tonry, J. L., Dressler, A., Blakeslee, J. P., Ajhar, E. A., Fletcher, A. B., Luppino, G. A., Metzger, M. R., & Moore, C. B. 2001, *ApJ*, 546, 681
- Trager, S. C., Worthey, G., Faber, S. M., Burstein, D., & Gonzalez, J. J. 1998, *ApJS*, 116, 1
- Tremonti, C. A., Heckman, T. M., Kauffmann, G., Brinchmann, J., Charlot, S., White, S. D. M., Seibert, M., Peng, E. W., et al. 2004, *ApJ*, 613, 898
- Tully, R. B. 1988, *Nearby galaxies catalog* (Cambridge and New York, Cambridge University Press, 1988, 221 p.)

- Tully, R. B., Verheijen, M. A. W., Pierce, M. J., Huang, J., & Wainscoat, R. J. 1996, *AJ*, 112, 2471
- Turner, A. M. 1998, Ph.D. Thesis
- van Dokkum, P. G. 2001, *PASP*, 113, 1420
- Veilleux, S., Kim, D.-C., & Sanders, D. B. 1999, *ApJ*, 522, 113
- Veilleux, S., Kim, D.-C., Sanders, D. B., Mazzarella, J. M., & Soifer, B. T. 1995, *ApJS*, 98, 171
- Vorontsov-Vel'Yaminov, B. A., & Arkhipova, V. P. 1962, in *Morphological catalogue of galaxies.*, 1 (1962), 0–+
- Witt, A. N., & Gordon, K. D. 2000, *ApJ*, 528, 799
- Worthey, G., Faber, S. M., Gonzalez, J. J., & Burstein, D. 1994, *ApJS*, 94, 687
- Worthey, G., & Ottaviani, D. L. 1997, *ApJS*, 111, 377
- Wu, W., Clayton, G. C., Gordon, K. D., Misselt, K. A., Smith, T. L., & Calzetti, D. 2002, *ApJS*, 143, 377
- York, D. G., et al. 2000, *AJ*, 120, 1579
- Zaritsky, D., Harris, J., Thompson, I. B., Grebel, E. K., & Massey, P. 2002, *AJ*, 123, 855

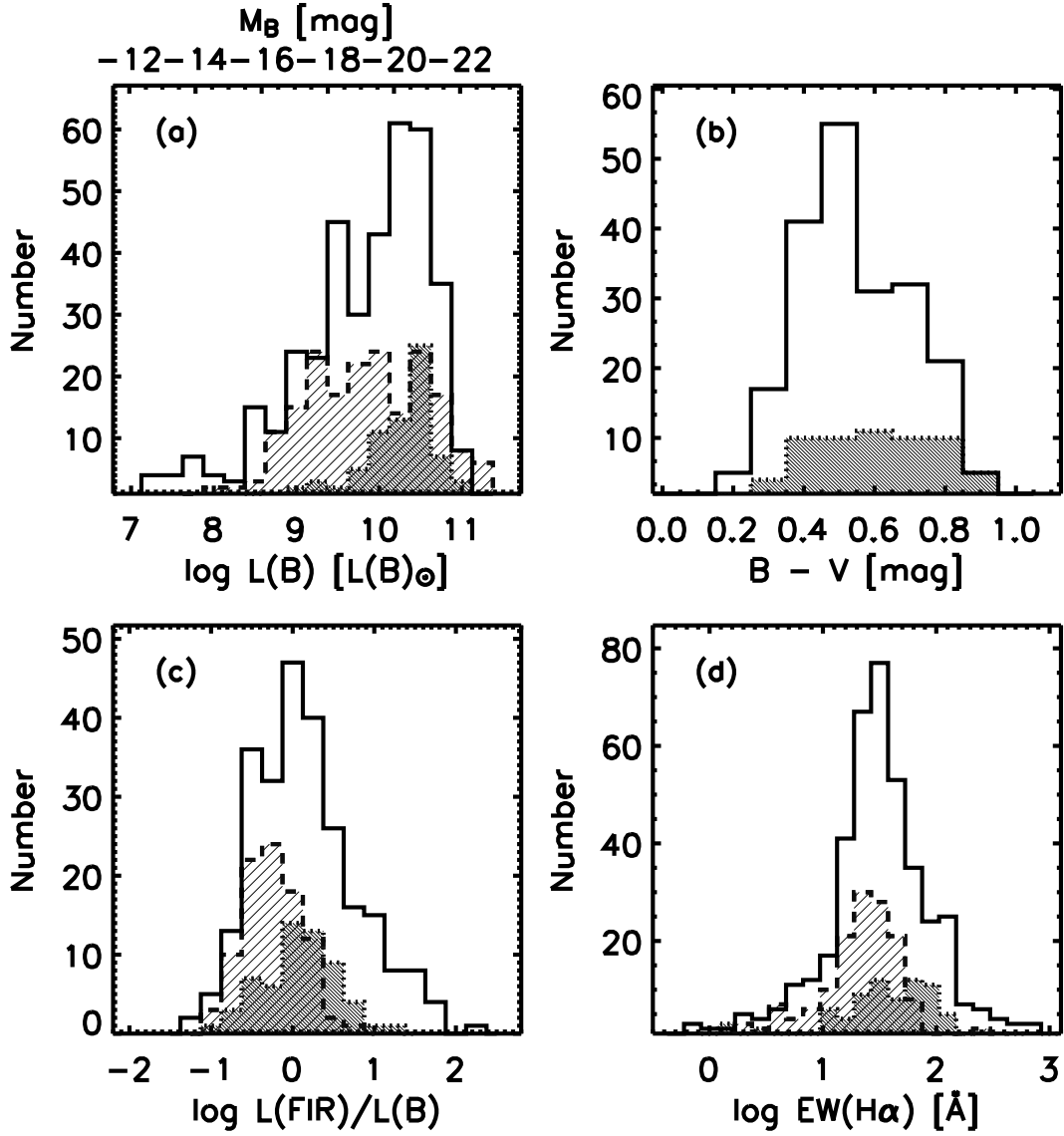


Fig. 1.— Comparison of the distribution of physical properties for our survey (*solid-line* open histogram), the K92 spectral atlas (*dotted-line*, dark grey histogram; Kennicutt 1992a,b), and the NFGS (*dashed-line*, light grey histogram; Jansen et al. 2000a,b). (a) B-band luminosity,  $L(B)$ , where we use  $M_{\odot,B} = +5.42$  mag to convert between  $L(B)/L(B)_\odot$  and  $M_B$ ; (b)  $B - V$  color; (c) far-infrared (FIR) to B-band luminosity ratio,  $L(\text{FIR})/L(B)$ ; and (d) equivalent width of  $\text{H}\alpha$   $\lambda 6563$ ,  $\text{EW}(\text{H}\alpha)$ . In panel (d),  $\text{EW}(\text{H}\alpha)$  for our sample (see §4) and the NFGS (see Jansen et al. (2000a)) have been corrected for underlying stellar absorption; no absorption corrections have been applied to the K92 measurements, and, following Kennicutt (1992b), we adopt a constant  $[\text{N II}]/\text{H}\alpha = 0.5$  ratio to convert from  $\text{EW}(\text{H}\alpha + [\text{N II}])$  to  $\text{EW}(\text{H}\alpha)$ .

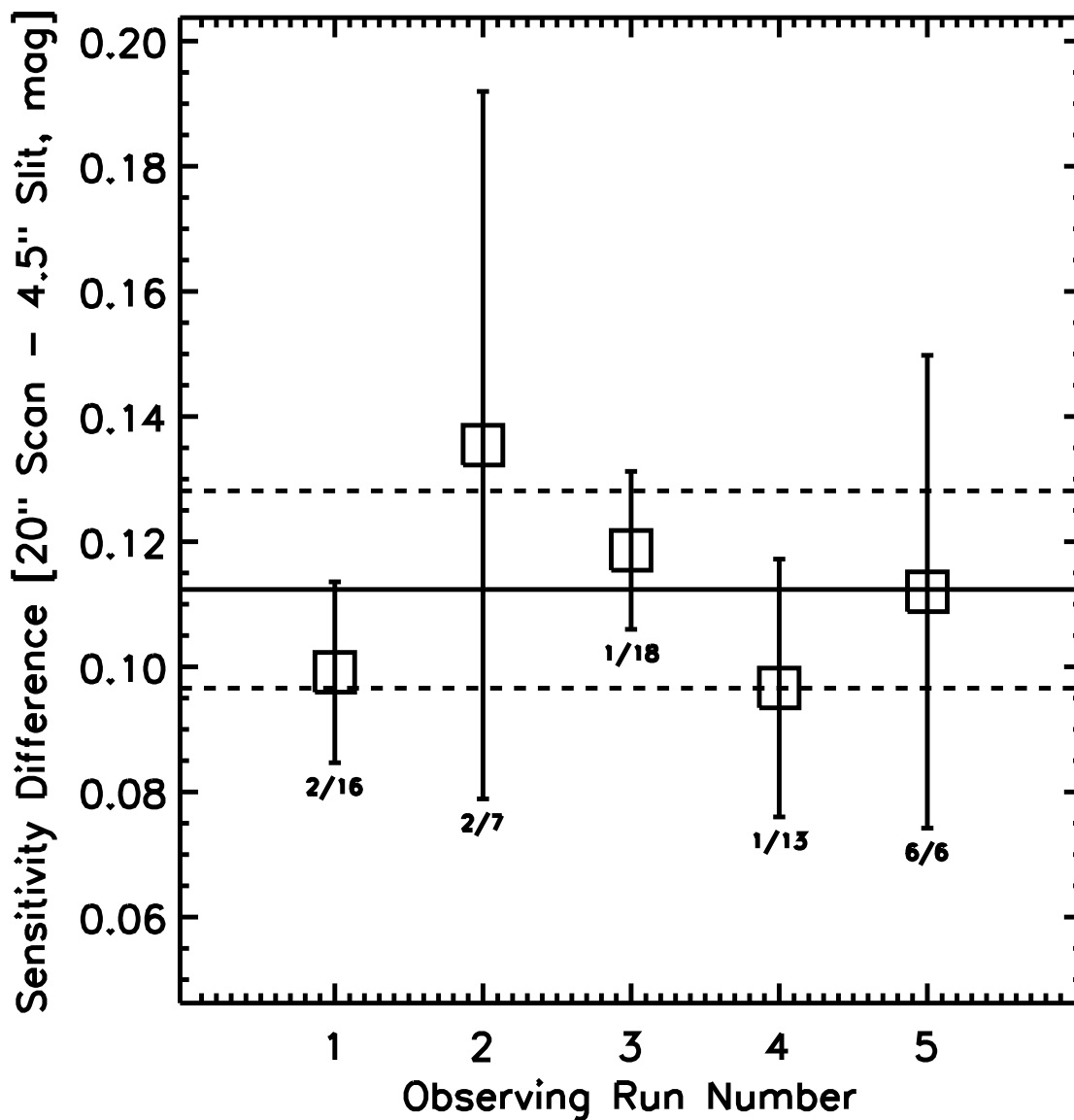


Fig. 2.— Measured magnitude difference near  $\sim 5500 \text{ \AA}$  between the  $20''$  drift-scanned and  $4.5''$ -slit sensitivity functions for 5 separate observing runs. This figure quantifies the correction needed to account for light missed by the  $4.5''$  slit due to seeing. The unweighted mean magnitude correction is  $0.11 \pm 0.02$  mag. The pair of numbers below each measurement, for example 2/7, give the numbers of standard stars used to construct the drift-scanned sensitivity function (2) and the  $4.5''$  sensitivity function (7), respectively. The error bar for each point is the quadrature sum of the observed uncertainty in each contributing sensitivity function.

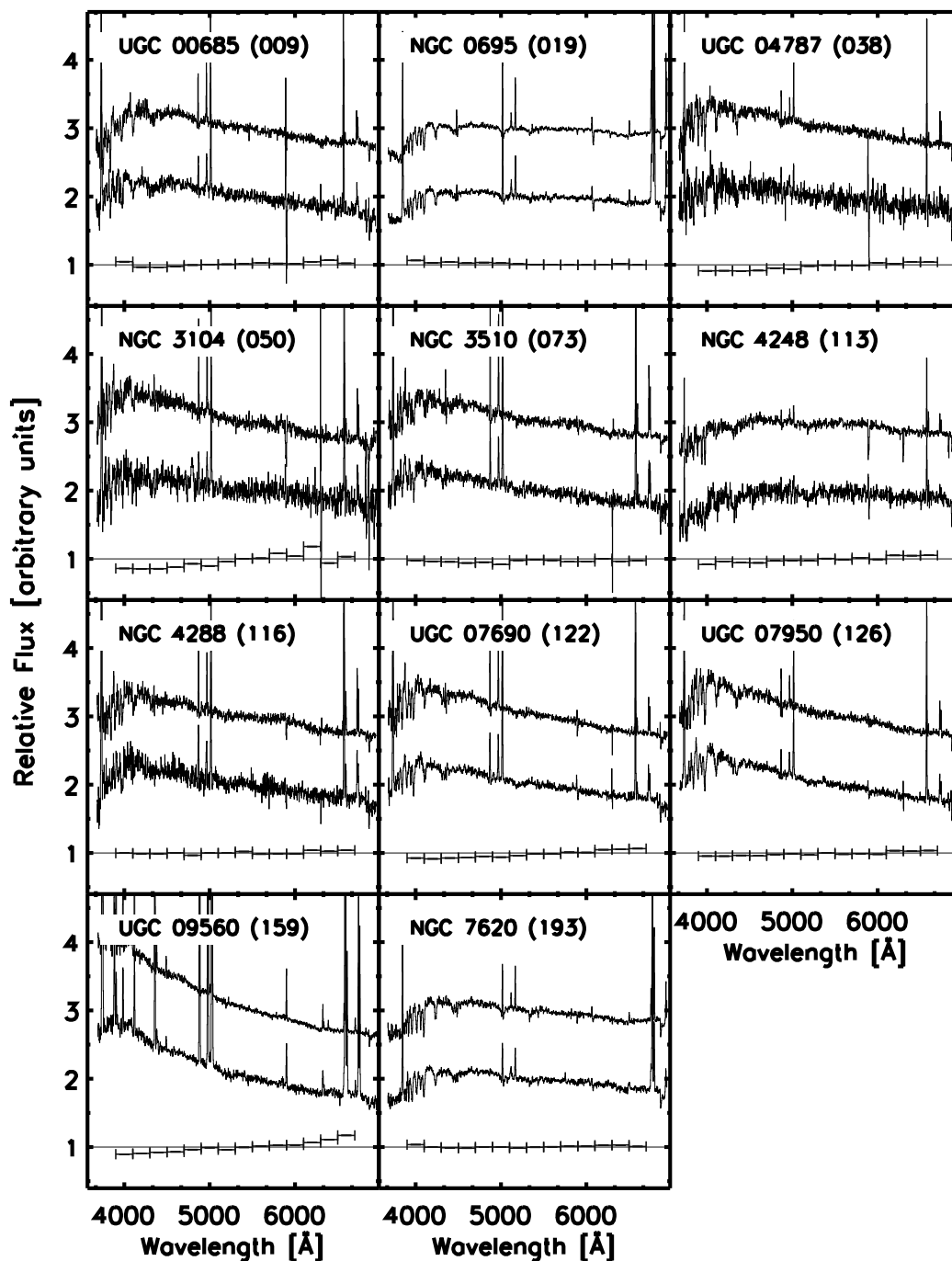


Fig. 3.— Comparison of the 11 galaxies in common with the Nearby Field Galaxy Survey (NFGS; Jansen et al. 2000b). Each object is identified by the galaxy name listed in Table 1 and the corresponding NFGS identification number in parenthesis. We normalize the spectra to the mean flux around  $5500 \pm 50 \text{ \AA}$  and offset each NFGS spectrum one unit upwards for clarity. The ratio of the two spectra are plotted in  $200\text{-\AA}$  wide bins to illustrate the differences in continuum shape.

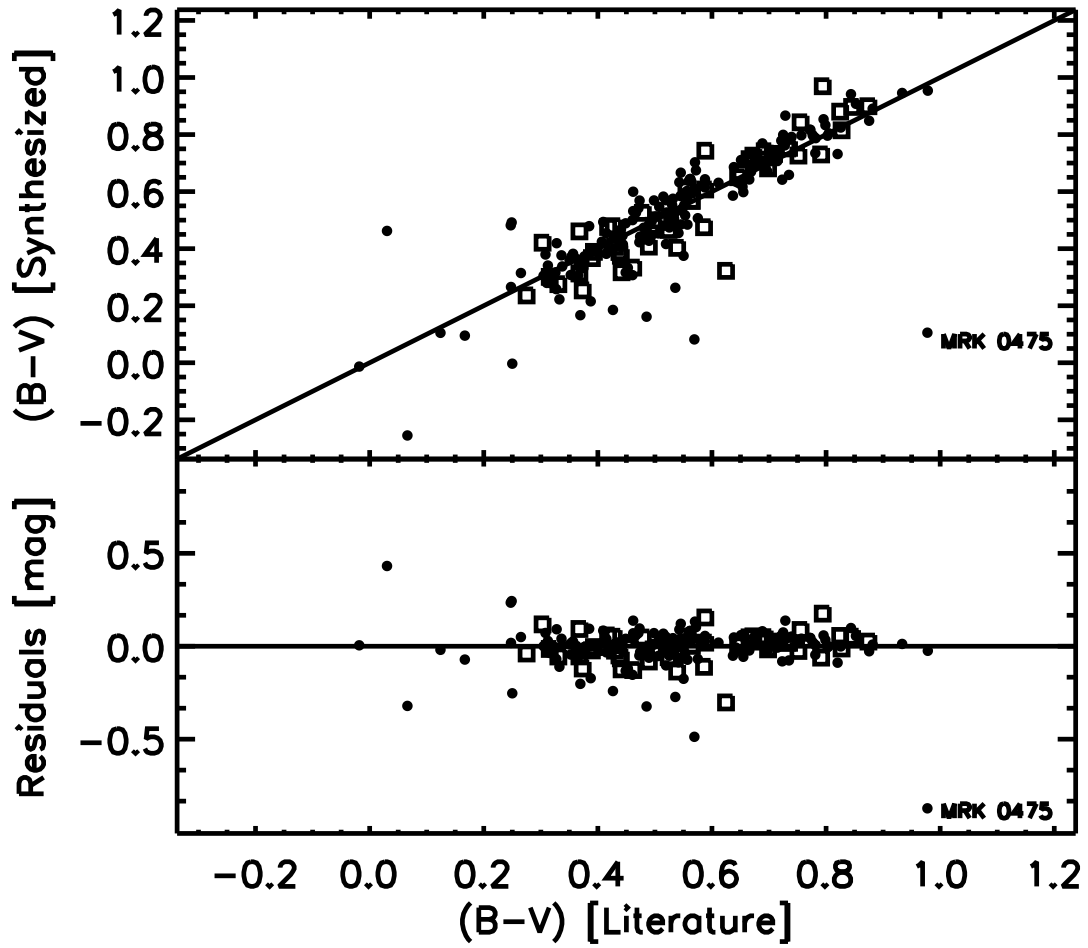


Fig. 4.— Comparison of our synthesized  $B-V$  colors against the literature. We plot galaxies observed during clear and non-photometric conditions using filled circles and open squares, respectively. We label Mrk 0475, the largest significant outlier, in both panels and discuss it in §2.5.

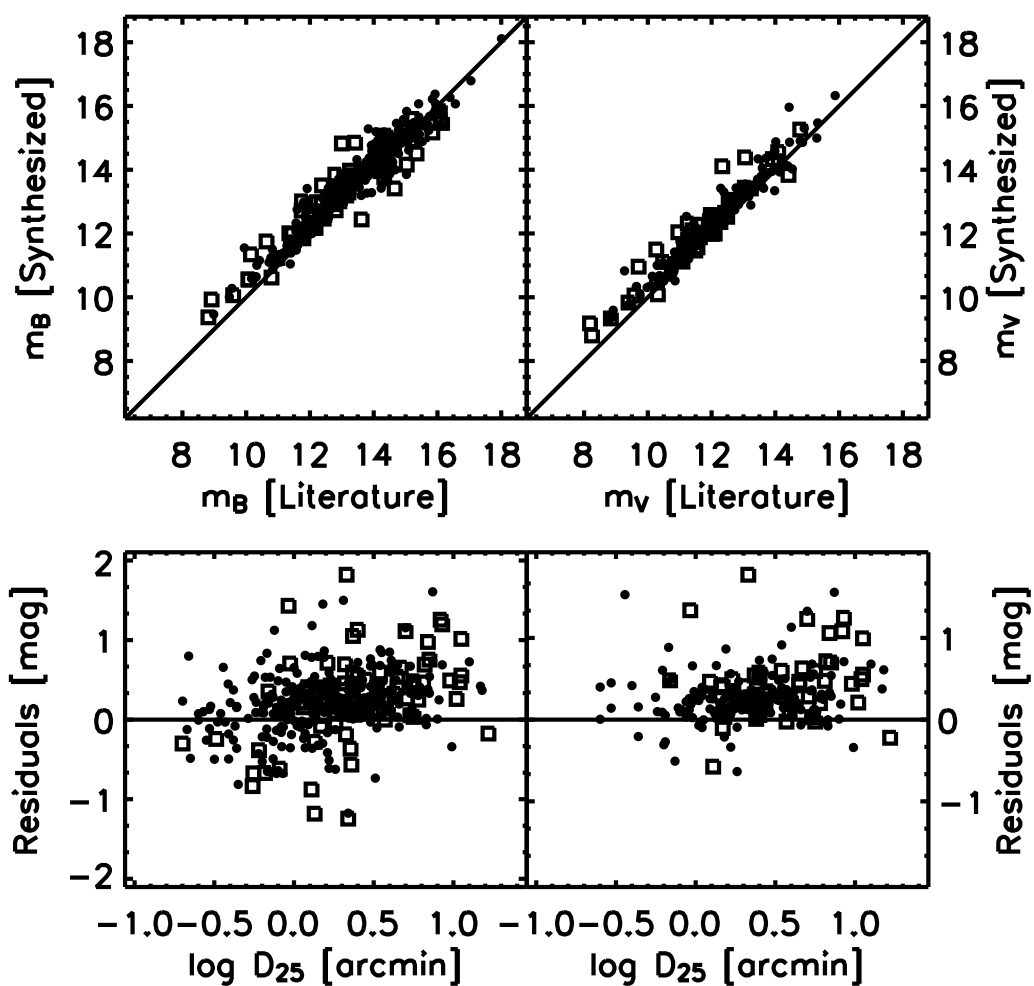


Fig. 5.— Comparison of apparent magnitudes synthesized directly from our spectra against literature measurements in the B- (*left*) and V-band (*right*). The bottom panel shows the magnitude residuals versus  $D_{25}$ , the 25 mag arcsec<sup>-2</sup> isophotal diameter of the major axis in arcminutes. Points are coded as in Figure 4.

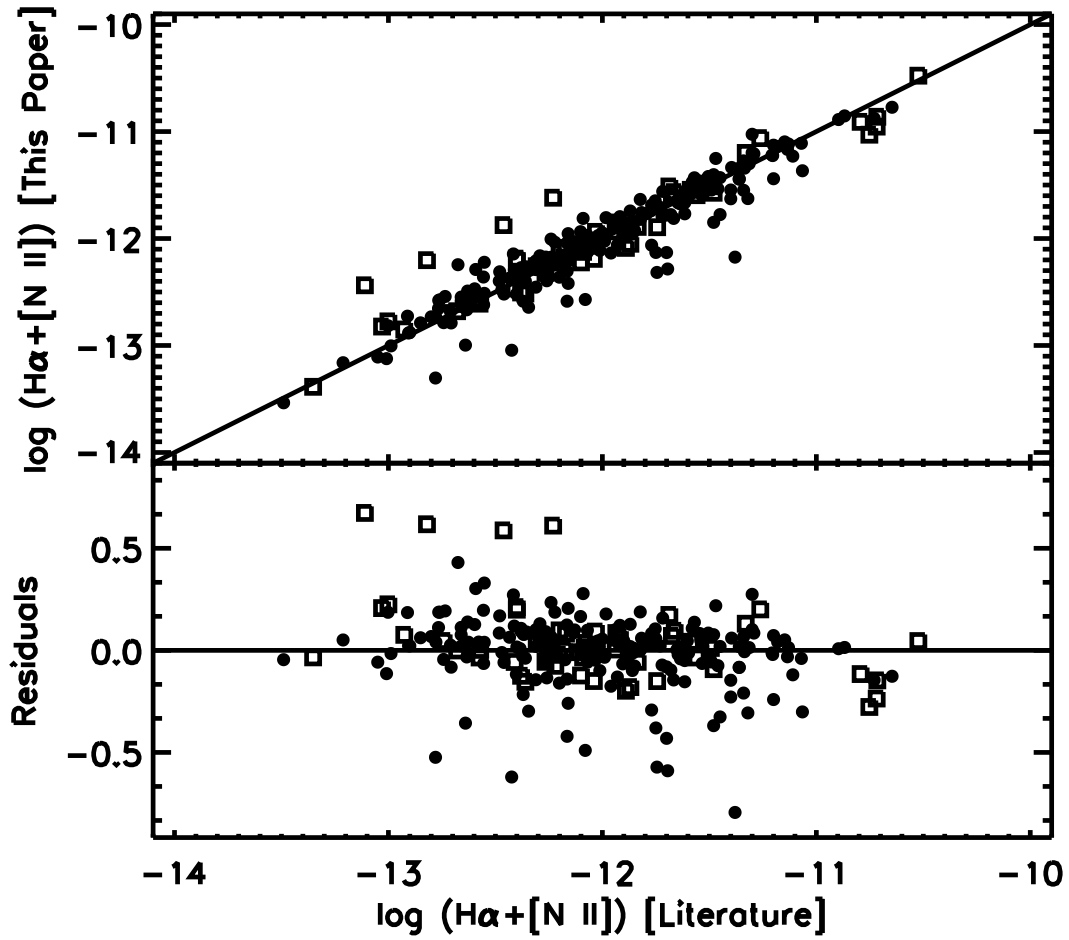


Fig. 6.— Comparison of our integrated spectrophotometric  $H\alpha+[N II] \lambda\lambda 6548, 6584$  emission-line fluxes in  $\text{erg s}^{-1} \text{cm}^{-2} \text{\AA}^{-1}$  against measurements in the literature using the symbols defined in Figure 4.

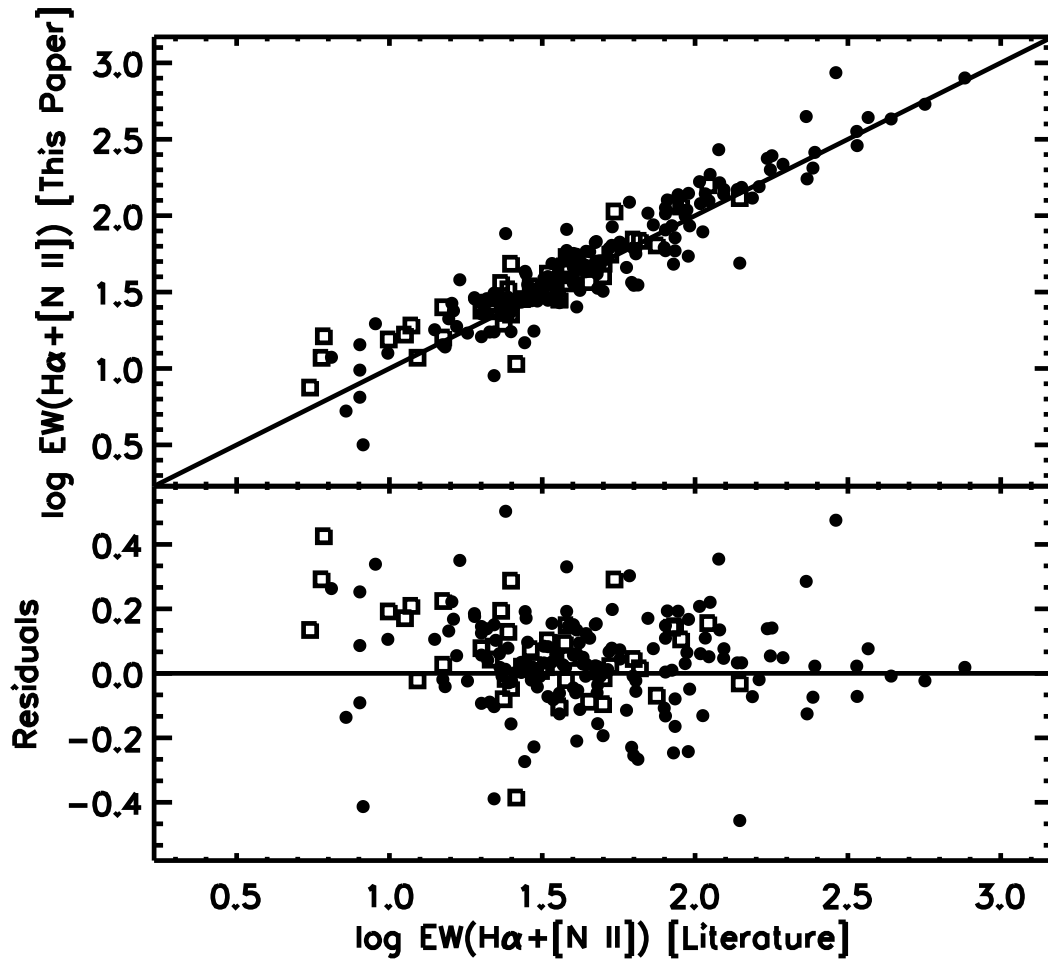


Fig. 7.— Comparison of  $\text{H}\alpha + [\text{N II}]$   $\lambda\lambda 6548, 6584$  equivalent width measurements in Angstroms from our integrated spectrophotometry against the literature values with the individual points coded as in Figure 4.

**Fig. Set 8. Spectral Visualizations**

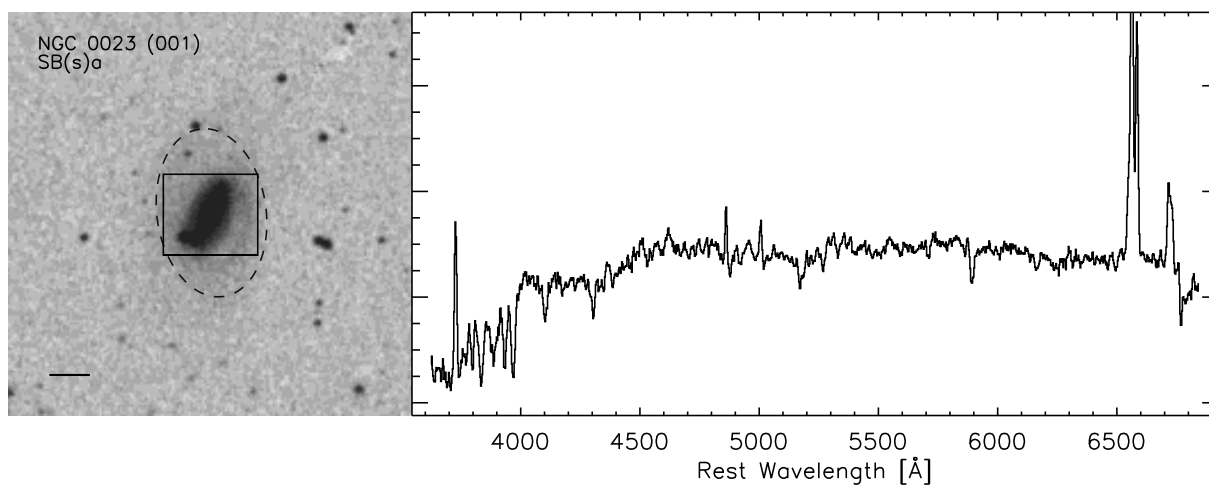


Fig. 8.1.— Presentation of our integrated spectral atlas. We plot the spectrum as  $f_{\lambda}(\lambda)$  versus rest wavelength, normalized in a way that attempts to achieve a balance between showing the full range in flux and illustrating the finer details of the continuum. Our integrated spectrum is accompanied by a Digitized Sky Survey image which illustrates our rectangular spectroscopic aperture as a *solid* outline and the 25 mag arcsec<sup>-2</sup> isophotal size of the galaxy as a *dashed* ellipse. The image legend gives the galaxy name, the unique identification number in parenthesis, and the morphological type as listed in Table 1. The horizontal solid line in the lower-left corner of each image represents 30". [See the electronic edition of the *Astrophysical Journal* for Figs. 8.2-8.417.]

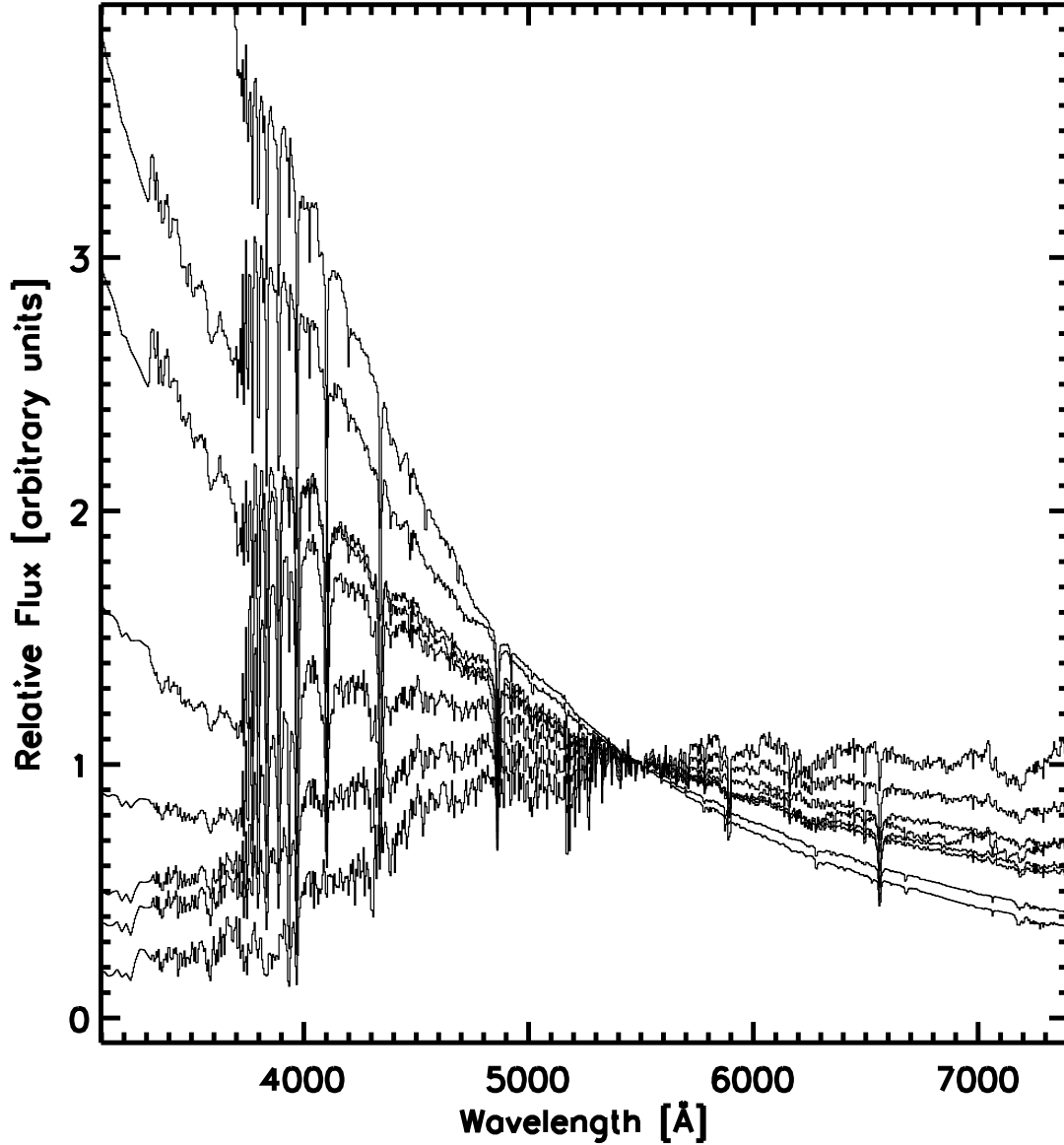


Fig. 9.— The eight instantaneous-burst, solar metallicity population synthesis models from Bruzual & Charlot (2003), normalized at  $5500 \text{ \AA}$ , that we use to model the stellar continuum of each galaxy. Each spectrum corresponds to the following ages, plotted from top to bottom on the left-hand side of the figure: 0, 5, 25, 100, 255, 640, 1400, and 12000 Myr. The FWHM spectral resolution of these models is  $3 \text{ \AA}$ .

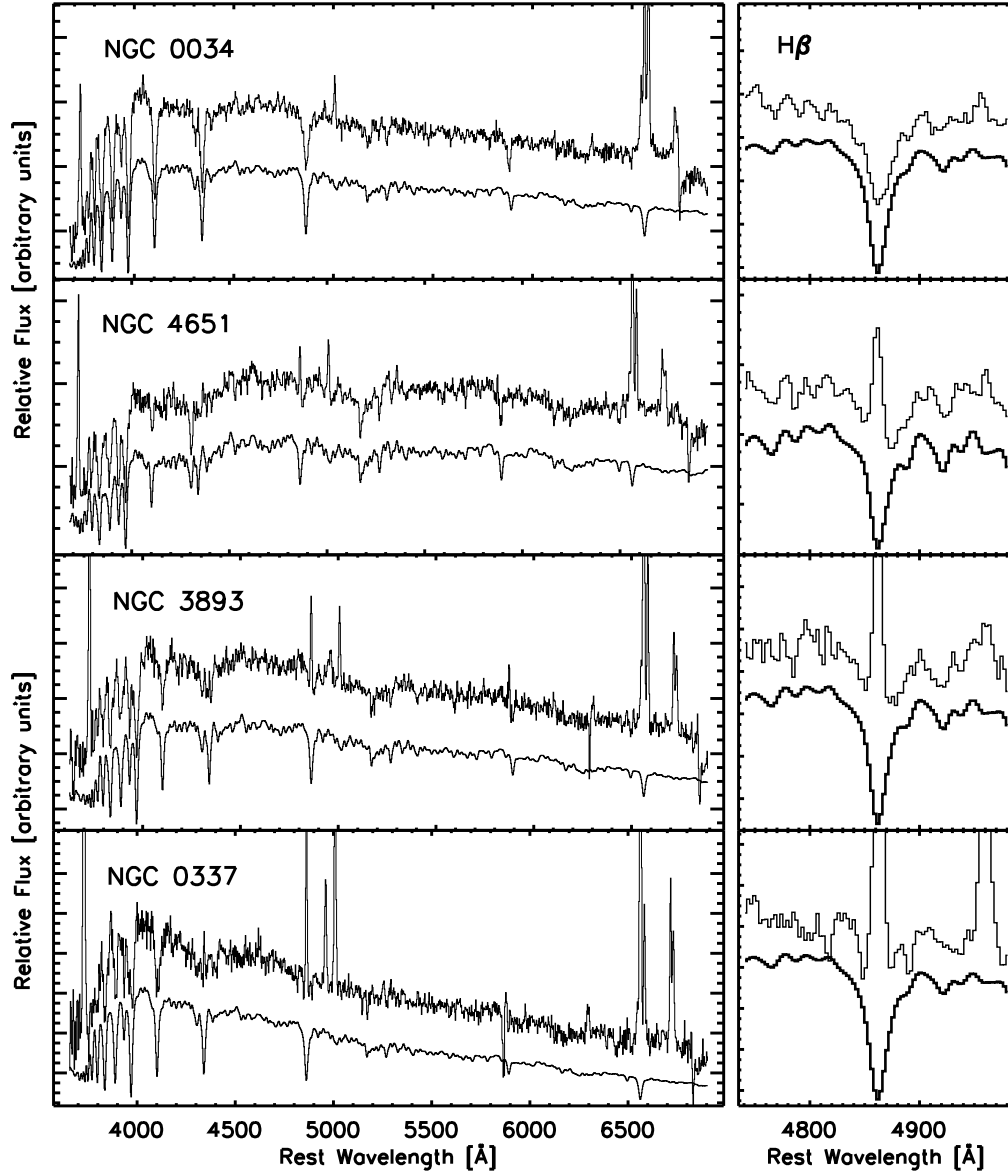


Fig. 10.— Illustration of our population synthesis fitting technique for the integrated spectra of NGC 0034, NGC 4651, NGC 3893, and NGC 0337. For each object we offset the best-fitting stellar continuum spectrum downward from the data for clarity. The left panels show the full spectral range while the right panel zooms in on the H $\beta$   $\lambda$ 4861 nebular emission line.

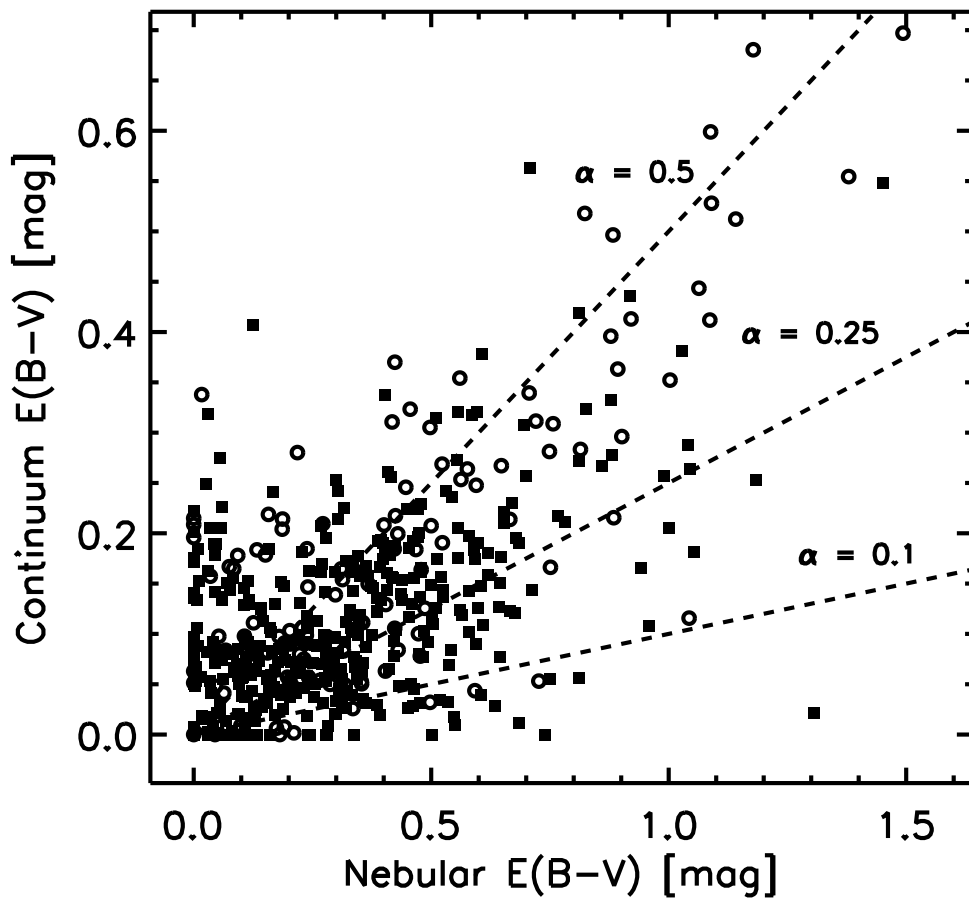


Fig. 11.— Correlation between the best-fitting continuum reddening,  $E(B-V)$ , and the nebular reddening as derived from the  $H\alpha/H\beta$  Balmer decrement for our nuclear spectra (open circles) and our integrated spectra (filled squares). The dashed lines show three values of the  $\alpha$  parameter, assuming that the nebular reddening traces the reddening of the young ( $< 10$  Myr) stellar populations. See §3.4 for more details.

Table 1. General Properties

ID (1)	Galaxy Name (2)	Other Names (3)	$\alpha_{J2000.0}$ (4)	$\delta_{J2000.0}$ (5)	$cz$ (6)	$E(B-V)$ (7)	Type (8)	$D_{25}^{\text{maj}}$ (9)	$D_{25}^{\text{min}}$ (10)	$\theta$ (11)	D (12)	Ref. (13)
001	NGC 0023	UGC 00089, MRK 0545	00:09:53.4	+25:55:26	4556	0.038	SB(s)a	2.09	1.35	8	64.2	1
002	NGC 0034	NGC 0017, MRK 0938	00:11:06.5	-12:06:26	5935	0.027	Sc	2.19	0.81	31 <sup>b</sup>	83.2	1
003	ARP 256 N	MCG -02-01-052	00:18:50.1	-10:21:42	8184	0.036	SB(s)c	1.12	0.76	50 <sup>b</sup>	114.3	1
004	ARP 256	VV 352	00:18:50.4	-10:22:08	8154	0.036	Pec	...	...	...	113.9	1
005	ARP 256 S	MCG -02-01-051	00:18:50.9	-10:22:37	8124	0.036	SB(s)b	1.10	0.63	71 <sup>b</sup>	113.4	1
006	NGC 0095	UGC 00214	00:22:13.5	+10:29:30	5366	0.116	SAB(rs)c	1.95	1.12	87 <sup>b</sup>	74.9	1
007	NGC 0151	NGC 0153	00:34:02.8	-09:42:19	3747	0.032	SB(r)bc	3.71	1.70	75	52.5	1
008	NGC 0157	MCG -02-02-056	00:34:46.7	-08:23:47	1678	0.044	SAB(rs)bc	4.17	2.69	30	24.0	1
009	NGC 0178	IC 0039, VIII Zw 034	00:39:08.4	-14:10:22	1439	0.021	SB(s)m	2.04	0.98	175	20.7	1
010	NGC 0232	MCG -04-02-040	00:42:45.8	-23:33:41	6655	0.019	SB(r)a	0.95	0.78	13 <sup>b</sup>	93.3	1

Note. — Col. (1) ID number; Col. (2) Galaxy name; Col. (3) Other common galaxy name or names; Col. (4) Right ascension from NED, unless otherwise noted (J2000); Col. (5) Declination from NED, unless otherwise noted (J2000); Col. (6) Heliocentric redshift from NED ( $\text{km s}^{-1}$ ); Col. (7) Foreground Galactic reddening from Schlegel et al. (1998) (mag); Col. (8) Morphological type (see §2.2); Col. (9) Major axis diameter at the 25 mag  $\text{arcsec}^{-2}$  isophote from the RC3, unless otherwise noted (arcmin); Col. (10) Minor axis diameter at the 25 mag  $\text{arcsec}^{-2}$  isophote from the RC3, unless otherwise noted (arcmin); Col. (11) Position angle, measured positive from North to East from the RC3, unless otherwise noted (deg); Col. (12) Distance (Mpc); Col. (13) Distance reference. Table 1 is published in its entirety in the electronic edition of the *Astrophysical Journal*. A portion is shown here for guidance regarding its form and content.

<sup>a</sup>Coordinates taken from SIMBAD.

<sup>b</sup>Coordinates, major/minor axis diameters, and/or position angle taken from LEDA.

<sup>c</sup>Major/minor axis diameter from NED "Basic Data".

<sup>d</sup>Major/minor axis diameter and/or position angle from the Uppsala General Catalog of Galaxies (UGC; Nilson 1973).

<sup>e</sup>Major/minor axis diameter and/or position angle from the ESO/Uppsala Survey of the ESO(B) Atlas (Lauberts 1982).

<sup>f</sup>Major/minor axis diameter and/or position angle from the Morphological Catalogue of Galaxies (MCG; Vorontsov-Vel'Yaminov & Arkhipova 1962).

<sup>g</sup>Position angle from the 2MASS Large Galaxy Atlas (Jarrett et al. 2003).

<sup>h</sup>Position angle from the 2MASS Extended Source Catalog (Jarrett et al. 2000).

References. — (1) Mould et al. (2000); (2) Karachentsev et al. (2004); (3) Shapley et al. (2001); (4) Freedman et al. (2001); (5) Tully et al. (1996); (6) Tonry et al. (2001)

Table 2. Photometric Properties

ID (1)	U (2)	B (3)	V (4)	J (5)	H (6)	K <sub>s</sub> (7)	S <sub>ν</sub> (12 μm) (8)	S <sub>ν</sub> (25 μm) (9)	S <sub>ν</sub> (60 μm) (10)	S <sub>ν</sub> (100 μm) (11)
001	...	12.69 ± 0.17	11.91 ± 0.18	9.877 ± 0.013	9.188 ± 0.014	8.862 ± 0.020	0.590 ± 0.042	1.240 ± 0.054	8.770 ± 0.047	14.960 ± 0.096
002	...	15.03 ± 0.46	...	11.216 ± 0.025	10.449 ± 0.029	10.064 ± 0.030	0.360 ± 0.038	2.380 ± 0.066	16.080 ± 0.058	16.97 ± 0.20
003	...	14.70 ± 0.15	...	12.656 ± 0.052	12.329 ± 0.088	11.811 ± 0.092	...	...	...	...
004	...	...	...	...	...	...	0.230 ± 0.040	1.180 ± 0.066	7.350 ± 0.046	9.48 ± 0.16
005	...	14.66 ± 0.13	14.22 ± 0.13	12.404 ± 0.028	11.677 ± 0.037	11.330 ± 0.046	...	...	...	...
006	12.67 ± 0.14	12.71 ± 0.14	12.16 ± 0.15	10.246 ± 0.020	9.642 ± 0.025	9.407 ± 0.033	0.127 ± 0.033	0.190 ± 0.053	2.20 ± 0.15	5.28 ± 0.48
007	12.28 ± 0.13	12.18 ± 0.13	11.49 ± 0.13	9.520 ± 0.015	8.929 ± 0.022	8.741 ± 0.030	0.215 ± 0.039	0.255 ± 0.051	1.53 ± 0.11	5.58 ± 0.61
008	10.76 ± 0.12	10.82 ± 0.12	10.27 ± 0.12	8.5600 ± 0.0060	7.8970 ± 0.0080	7.665 ± 0.012	1.570 ± 0.044	2.080 ± 0.059	17.570 ± 0.045	43.10 ± 0.12
009	12.65 ± 0.21	13.01 ± 0.20	12.56 ± 0.20	11.670 ± 0.036	11.085 ± 0.050	10.794 ± 0.065	...	...	1.62 ± 0.13	2.59 ± 0.21
010	...	14.31 ± 0.21	...	10.968 ± 0.025	10.275 ± 0.028	9.889 ± 0.030	0.360 ± 0.042	1.220 ± 0.040	10.060 ± 0.036	16.83 ± 0.11

Note. — Col. (1) ID number; Col. (2) U magnitude; Col. (3) B magnitude; Col. (4) V magnitude; Col. (5) 2MASS total J magnitude; Col. (6) 2MASS total H magnitude; Col. (7) 2MASS total K<sub>s</sub> magnitude; Col. (8) IRAS 12 μm flux density (Jy); Col. (9) IRAS 25 μm flux density (Jy); Col. (10) IRAS 60 μm flux density (Jy); Col. (11) IRAS 100 μm flux density (Jy). Table 2 is published in its entirety in the electronic edition of the *Astrophysical Journal*. A portion is shown here for guidance regarding its form and content.

<sup>a</sup>Soifer et al. (1989) do not provide measurement errors for the IRAS fluxes of NGC 5194, therefore we assume a fixed 25% uncertainty at every wavelength.

Table 3. Summary of Integrated Spectrophotometric Observations

ID (1)	Galaxy name (2)	$\Delta_{\text{scan}}$ (3)	Ap. (4)	$\theta_{\text{slit}}$ (5)	$t$ (6)	Clear (7)	$\Delta m$ (8)	Remarks <sup>a</sup> (9)
001	NGC 0023	60	70	90	1800	Y	0.054	supernova 1955C subtracted
002	NGC 0034	40	45	90	1800	Y	0.054	
003	ARP 256 N	40	60	180	1800	Y	0.054	interacting with ARP 256 S
004	ARP 256	40	100	180	1800	Y	0.054	interacting pair
005	ARP 256 S	40	40	180	1800	Y	0.054	interacting with ARP 256 N
006	NGC 0095	60	100	90	2400	Y	0.054	
007	NGC 0151	150	120	180	2400	N	0.531	
008	NGC 0157	180	130	90	2400	Y	0.054	foreground star excluded
009	NGC 0178	90	60	90	2400	Y	0.054	
010	NGC 0232	40	60	90	3600	Y	0.078	

Note. — Col. (1) ID number; Col. (2) Galaxy name; Col. (3) Drift scan length perpendicular to the slit (arcsec); Col. (4) Extraction aperture along the slit (arcsec); Col. (5) Slit position angle measured positive from North to East (deg); Col. (6) Total exposure time (seconds); Col. (7) Flag indicating clear (Y) or non-photometric (N) observing conditions; Col. (8) Absolute spectrophotometric uncertainty ( $1\sigma$ ) based only on the scatter in the observed sensitivity function (mag); Col. (9) Remarks regarding the object or the spectral extraction. Table 3 is published in its entirety in the electronic edition of the *Astrophysical Journal*. A portion is shown here for guidance regarding its form and content.

<sup>a</sup>In this footnote we clarify some of the remarks that appear in column (9): *stellar contamination*: indicates foreground stellar contamination that could not be subtracted; *foreground star(s) excluded*: a smaller extraction aperture was adopted to avoid one or more foreground stars; *scan avoids star(s)*: the drift scan center and length were selected to avoid nearby bright stars.

<sup>b</sup>Variance-weighted average of three indistinguishable spectra extracted using  $80'' \times 25''$  (PA=180°),  $80'' \times 60''$  (PA=180°), and  $80'' \times 60''$  (PA=90°) apertures.

<sup>c</sup>Variance-weighted average of two indistinguishable spectra obtained at a 90° slit position angle and extracted using  $110'' \times 60''$  and  $110'' \times 100''$  apertures.

<sup>d</sup>Variance-weighted average of two indistinguishable spectra obtained at a 90° slit position angle and extracted using  $90'' \times 360''$  and  $100'' \times 360''$  apertures.

<sup>e</sup>Variance-weighted average of two indistinguishable spectra extracted using  $160'' \times 60''$  (PA=70°) and  $140'' \times 90''$  (PA=90°) apertures.

<sup>f</sup>Variance-weighted average of two indistinguishable spectra obtained at a 90° slit position angle and extracted using  $80'' \times 40''$  and  $80'' \times 50''$  apertures.

<sup>g</sup>Variance-weighted average of two indistinguishable spectra taken at 114° and 108°.

<sup>h</sup>Variance-weighted average of two indistinguishable spectra extracted using  $125'' \times 30''$  (PA=165°) and  $60'' \times 60''$  (PA=90°) apertures.

<sup>i</sup>Variance-weighted average of three indistinguishable spectra obtained at a 90° slit position angle and extracted using  $140'' \times 60''$  and two  $140'' \times 75''$  apertures.

<sup>j</sup>Variance-weighted average of two indistinguishable spectra extracted using  $75'' \times 150''$  (PA=90°) and  $95'' \times 155''$  (PA=180°) apertures.

<sup>k</sup>Variance-weighted average of two indistinguishable spectra extracted using  $40'' \times 150''$  (PA=90°) and  $45'' \times 155''$  (PA=180°) apertures.

<sup>l</sup>Variance-weighted average of two indistinguishable spectra extracted using  $35'' \times 150''$  (PA=90°) and  $50'' \times 155''$  (PA=180°) apertures.

<sup>m</sup>Variance-weighted average of three indistinguishable spectra extracted using  $90'' \times 20''$  (PA=130°),  $90'' \times 20''$  (PA=130°), and  $50'' \times 30''$  (PA=90°) apertures.

<sup>n</sup>Variance-weighted average of two indistinguishable spectra obtained at a 90° slit position angle and extracted using  $45'' \times 10''$  and  $45'' \times 20''$  apertures.

<sup>o</sup>Variance-weighted average of two indistinguishable spectra obtained at a 90° slit position angle and extracted using  $50'' \times 30''$  and  $50'' \times 40''$  apertures.

<sup>p</sup>Variance-weighted average of two indistinguishable spectra taken at 90° and 153°.

Table 4. Integrated Emission-line Fluxes<sup>a</sup>

ID	[O II] $\lambda$ 3727	H $\delta$ $\lambda$ 4101	H $\gamma$ $\lambda$ 4340	H $\beta$ $\lambda$ 4861	[O III] $\lambda$ 5007	[O I] $\lambda$ 6300	H $\alpha$ $\lambda$ 6563	[N II] $\lambda$ 6584	[S II] $\lambda$ 6716	[S II] $\lambda$ 6731
001	352 $\pm$ 30	64.2 $\pm$ 6.1	95.5 $\pm$ 6.1	223.0 $\pm$ 9.9	97.9 $\pm$ 5.8	32.9 $\pm$ 5.0	1158 $\pm$ 47	603 $\pm$ 25	219 $\pm$ 11	149.8 $\pm$ 9.4
002	124 $\pm$ 17	9.9 $\pm$ 3.0	7.3 $\pm$ 2.6	23.5 $\pm$ 2.3	44.5 $\pm$ 2.9	18.7 $\pm$ 2.7	203.7 $\pm$ 9.1	220.5 $\pm$ 9.6	62.6 $\pm$ 4.1	12.7 $\pm$ 3.6
003	233 $\pm$ 18	20.5 $\pm$ 2.9	43.9 $\pm$ 3.0	106.3 $\pm$ 4.8	92.8 $\pm$ 4.4	17.8 $\pm$ 2.6	400 $\pm$ 16	115.9 $\pm$ 5.4	60.1 $\pm$ 3.7	34.9 $\pm$ 3.2
004	571 $\pm$ 32	50.7 $\pm$ 4.3	102.8 $\pm$ 5.3	260 $\pm$ 11	230.7 $\pm$ 9.8	46.8 $\pm$ 3.9	1103 $\pm$ 44	344 $\pm$ 14	167.8 $\pm$ 7.8	110.8 $\pm$ 6.0
005	336 $\pm$ 20	30.2 $\pm$ 2.8	57.4 $\pm$ 3.2	152.0 $\pm$ 6.5	138.6 $\pm$ 6.0	28.9 $\pm$ 2.6	701 $\pm$ 28	227.2 $\pm$ 9.5	107.5 $\pm$ 5.1	76.8 $\pm$ 4.1
006	559 $\pm$ 42	72.4 $\pm$ 7.4	111.7 $\pm$ 7.3	225 $\pm$ 10	169.1 $\pm$ 8.3	41.3 $\pm$ 5.3	890 $\pm$ 36	315 $\pm$ 14	155.7 $\pm$ 9.6	112.6 $\pm$ 7.5
007	590 $\pm$ 110	146 $\pm$ 20	73 $\pm$ 17	309 $\pm$ 20	206 $\pm$ 18	< 48	971 $\pm$ 45	465 $\pm$ 29	214 $\pm$ 22	126 $\pm$ 21
008	1350 $\pm$ 120	431 $\pm$ 27	462 $\pm$ 25	1065 $\pm$ 45	326 $\pm$ 19	182 $\pm$ 18	4400 $\pm$ 180	1602 $\pm$ 67	893 $\pm$ 40	671 $\pm$ 32
009	880 $\pm$ 51	61.3 $\pm$ 6.1	111.7 $\pm$ 6.7	260 $\pm$ 11	641 $\pm$ 26	42.8 $\pm$ 5.1	844 $\pm$ 34	97.6 $\pm$ 5.8	181.1 $\pm$ 8.8	111.5 $\pm$ 6.6
010	64 $\pm$ 11	15.3 $\pm$ 2.2	8.7 $\pm$ 1.9	28.9 $\pm$ 2.1	31.9 $\pm$ 2.1	15.5 $\pm$ 2.2	235.1 $\pm$ 9.9	165.5 $\pm$ 7.2	< 16	< 16

Note. — Table 4 is published in its entirety in the electronic edition of the *Astrophysical Journal*. A portion is shown here for guidance regarding its form and content.

<sup>a</sup>Integrated emission-line fluxes in units of  $10^{-15}$  erg s $^{-1}$  cm $^{-2}$ . We give  $1\sigma$  upper limits assuming two significant figures and identify them using a < sign. These flux measurements have been corrected for foreground Galactic extinction using the reddening values in Table 1 and the O'Donnell (1994) Milky Way extinction curve assuming  $R_V = 3.1$ , as well as underlying stellar absorption as described in § 3.3. The errors only include statistical measurement uncertainties. We do not give fluxes for the following objects because their integrated spectra cannot be modeled reliably using the algorithm described in § 3: NGC 1275 (070), IRAS 05189-2524 (087), UGC 08058 (279), NGC 7469 (381), MRK 0315 (382), NGC 7674 (400), and ARP 182 (401).

Table 5. Nuclear Emission-line Fluxes<sup>a</sup>

ID	[O II] $\lambda$ 3727	H $\delta$ $\lambda$ 4101	H $\gamma$ $\lambda$ 4340	H $\beta$ $\lambda$ 4861	[O III] $\lambda$ 5007	[O I] $\lambda$ 6300	H $\alpha$ $\lambda$ 6563	[N II] $\lambda$ 6584	[S II] $\lambda$ 6716	[S II] $\lambda$ 6731
019	$7.9 \pm 1.1$	$0.59 \pm 0.16$	$1.23 \pm 0.15$	$2.56 \pm 0.16$	$1.19 \pm 0.13$	$0.38 \pm 0.12$	$7.47 \pm 0.36$	$1.99 \pm 0.16$	$2.21 \pm 0.18$	$1.71 \pm 0.16$
020	$0.88 \pm 0.56$	$< 0.08$	$0.166 \pm 0.069$	$0.283 \pm 0.062$	$0.183 \pm 0.063$	$< 0.06$	$1.03 \pm 0.10$	$< 0.07$	$0.233 \pm 0.080$	$0.190 \pm 0.079$
030	$4.24 \pm 0.99$	$1.10 \pm 0.36$	$< 2.8$	$< 1.8$	$1.63 \pm 0.25$	$1.01 \pm 0.29$	$6.53 \pm 0.65$	$7.78 \pm 0.54$	$1.99 \pm 0.35$	$2.04 \pm 0.36$
037	$9.72 \pm 0.96$	$1.16 \pm 0.16$	$1.95 \pm 0.16$	$4.84 \pm 0.24$	$4.10 \pm 0.22$	$0.53 \pm 0.14$	$22.94 \pm 0.96$	$5.73 \pm 0.29$	$3.90 \pm 0.24$	$2.71 \pm 0.20$
038	$2.80 \pm 0.80$	$1.24 \pm 0.19$	$1.66 \pm 0.18$	$3.93 \pm 0.23$	$1.17 \pm 0.17$	$0.51 \pm 0.19$	$28.4 \pm 1.2$	$11.44 \pm 0.55$	$\dots$	$\dots$
042	$0.46 \pm 0.45$	$< 0.09$	$0.107 \pm 0.070$	$0.186 \pm 0.061$	$0.228 \pm 0.060$	$< 0.1$	$0.518 \pm 0.090$	$0.062 \pm 0.058$	$0.247 \pm 0.072$	$0.134 \pm 0.066$
043	$< 0.27$	$< 0.2$	$0.21 \pm 0.17$	$0.34 \pm 0.15$	$0.45 \pm 0.16$	$< 0.19$	$4.30 \pm 0.31$	$2.22 \pm 0.21$	$0.59 \pm 0.20$	$0.57 \pm 0.20$
048	$< 0.81$	$0.51 \pm 0.27$	$< 0.63$	$< 0.45$	$< 0.63$	$< 0.97$	$2.83 \pm 0.43$	$< 0.84$	$< 1.1$	$\dots$
050	$2.33 \pm 0.96$	$0.60 \pm 0.22$	$0.26 \pm 0.20$	$0.59 \pm 0.19$	$1.26 \pm 0.22$	$0.42 \pm 0.26$	$5.04 \pm 0.42$	$5.34 \pm 0.43$	$1.58 \pm 0.32$	$1.27 \pm 0.32$
051	$2.54 \pm 0.86$	$0.96 \pm 0.19$	$1.19 \pm 0.17$	$3.22 \pm 0.21$	$3.45 \pm 0.23$	$0.70 \pm 0.20$	$30.6 \pm 1.3$	$13.10 \pm 0.60$	$5.08 \pm 0.34$	$4.27 \pm 0.31$

Note. — Table 5 is published in its entirety in the electronic edition of the *Astrophysical Journal*. A portion is shown here for guidance regarding its form and content.

<sup>a</sup>Nuclear emission-line fluxes in units of  $10^{-15}$  erg s<sup>-1</sup> cm<sup>-2</sup>. We give  $1\sigma$  upper limits assuming two significant figures and identify them using a  $<$  sign. These flux measurements have been corrected for foreground Galactic extinction using the reddening values in Table 1 and the O'Donnell (1994) Milky Way extinction curve assuming  $R_V = 3.1$ , as well as underlying stellar absorption as described in § 3.3. The errors only include statistical measurement uncertainties. We do not give fluxes for the following objects because their nuclear spectra cannot be modeled reliably using the algorithm described in § 3: NGC 1068 (054), NGC 1275 (070), NGC 3998 (214), NGC 4051 (223), and MRK 0315 (382).

Table 6. Integrated Emission-line Equivalent Widths<sup>a</sup>

ID	[O II] $\lambda$ 3727	H $\delta$ $\lambda$ 4101	H $\gamma$ $\lambda$ 4340	H $\beta$ $\lambda$ 4861	[O III] $\lambda$ 5007	[O I] $\lambda$ 6300	H $\alpha$ $\lambda$ 6563	[N II] $\lambda$ 6584	[S II] $\lambda$ 6716	[S II] $\lambda$ 6731
001	13.9 $\pm$ 1.2	1.52 $\pm$ 0.14	2.16 $\pm$ 0.14	4.44 $\pm$ 0.20	2.06 $\pm$ 0.12	0.70 $\pm$ 0.11	24.40 $\pm$ 0.99	12.66 $\pm$ 0.53	4.77 $\pm$ 0.24	3.29 $\pm$ 0.21
002	12.0 $\pm$ 1.6	0.50 $\pm$ 0.15	0.38 $\pm$ 0.13	1.22 $\pm$ 0.12	2.41 $\pm$ 0.16	1.17 $\pm$ 0.17	12.90 $\pm$ 0.58	13.57 $\pm$ 0.60	4.01 $\pm$ 0.28	0.86 $\pm$ 0.25
003	32.9 $\pm$ 2.7	2.26 $\pm$ 0.32	5.08 $\pm$ 0.35	12.66 $\pm$ 0.59	11.92 $\pm$ 0.58	2.71 $\pm$ 0.40	61.4 $\pm$ 2.6	17.38 $\pm$ 0.90	10.40 $\pm$ 0.80	6.34 $\pm$ 0.64
004	39.1 $\pm$ 2.3	2.67 $\pm$ 0.23	5.73 $\pm$ 0.30	15.16 $\pm$ 0.64	14.23 $\pm$ 0.61	3.54 $\pm$ 0.31	83.8 $\pm$ 3.5	25.4 $\pm$ 1.2	13.80 $\pm$ 0.82	9.78 $\pm$ 0.62
005	45.6 $\pm$ 3.0	3.07 $\pm$ 0.28	6.20 $\pm$ 0.35	17.47 $\pm$ 0.76	16.72 $\pm$ 0.73	4.33 $\pm$ 0.39	105.2 $\pm$ 4.4	33.8 $\pm$ 1.6	17.4 $\pm$ 1.0	12.69 $\pm$ 0.77
006	20.5 $\pm$ 1.7	1.58 $\pm$ 0.16	2.45 $\pm$ 0.16	4.73 $\pm$ 0.21	3.78 $\pm$ 0.19	1.06 $\pm$ 0.14	22.82 $\pm$ 0.94	7.96 $\pm$ 0.36	4.18 $\pm$ 0.28	3.31 $\pm$ 0.23
007	11.6 $\pm$ 2.2	1.77 $\pm$ 0.24	0.84 $\pm$ 0.19	3.12 $\pm$ 0.20	2.18 $\pm$ 0.20	< 0.56	11.23 $\pm$ 0.53	5.40 $\pm$ 0.34	2.60 $\pm$ 0.27	1.55 $\pm$ 0.26
008	11.5 $\pm$ 1.1	2.04 $\pm$ 0.13	2.19 $\pm$ 0.12	4.88 $\pm$ 0.21	1.603 $\pm$ 0.096	0.983 $\pm$ 0.099	23.72 $\pm$ 0.96	8.57 $\pm$ 0.36	4.83 $\pm$ 0.22	3.64 $\pm$ 0.18
009	34.0 $\pm$ 2.1	1.66 $\pm$ 0.16	3.29 $\pm$ 0.20	8.68 $\pm$ 0.38	22.76 $\pm$ 0.94	2.07 $\pm$ 0.25	43.4 $\pm$ 1.8	4.95 $\pm$ 0.30	9.38 $\pm$ 0.48	5.80 $\pm$ 0.35
010	13.1 $\pm$ 2.3	1.64 $\pm$ 0.24	0.84 $\pm$ 0.18	2.22 $\pm$ 0.16	2.50 $\pm$ 0.16	1.10 $\pm$ 0.15	15.97 $\pm$ 0.68	11.22 $\pm$ 0.49	< 1.1	< 1.2

Note. — Table 6 is published in its entirety in the electronic edition of the *Astrophysical Journal*. A portion is shown here for guidance regarding its form and content.

<sup>a</sup>Integrated rest-frame emission-line equivalent widths in Angstroms, corrected for underlying stellar absorption as described in § 3.3. We give  $1\sigma$  upper limits assuming two significant figures and identify them using a < sign. The errors only include statistical measurement uncertainties. We do not give equivalent widths for the following objects because their integrated spectra cannot be modeled reliably using the algorithm described in § 3: NGC 1275 (070), IRAS 05189-2524 (087), UGC 08058 (279), NGC 7469 (381), MRK 0315 (382), NGC 7674 (400), and ARP 182 (401).

Table 7. Nuclear Emission-line Equivalent Widths<sup>a</sup>

ID	[O II] $\lambda 3727$	H $\delta$ $\lambda 4101$	H $\gamma$ $\lambda 4340$	H $\beta$ $\lambda 4861$	[O III] $\lambda 5007$	[O I] $\lambda 6300$	H $\alpha$ $\lambda 6563$	[N II] $\lambda 6584$	[S II] $\lambda 6716$	[S II] $\lambda 6731$
019	$29.7 \pm 4.2$	$1.92 \pm 0.54$	$4.18 \pm 0.51$	$8.80 \pm 0.58$	$4.42 \pm 0.47$	$1.50 \pm 0.46$	$27.6 \pm 1.4$	$7.63 \pm 0.63$	$8.69 \pm 0.71$	$6.58 \pm 0.63$
020	$30 \pm 20$	$< 1.1$	$2.5 \pm 1.0$	$4.8 \pm 1.1$	$3.5 \pm 1.2$	$< 1.6$	$27.0 \pm 3.2$	$< 1.8$	$6.1 \pm 2.1$	$4.7 \pm 1.9$
030	$5.0 \pm 1.2$	$0.67 \pm 0.22$	$< 1.5$	$< 0.66$	$0.643 \pm 0.099$	$0.35 \pm 0.10$	$2.15 \pm 0.21$	$2.58 \pm 0.18$	$0.69 \pm 0.12$	$0.70 \pm 0.12$
037	$25.2 \pm 2.5$	$1.97 \pm 0.28$	$3.34 \pm 0.28$	$8.09 \pm 0.41$	$7.28 \pm 0.40$	$1.03 \pm 0.27$	$45.5 \pm 2.0$	$11.28 \pm 0.58$	$7.89 \pm 0.49$	$5.46 \pm 0.42$
038	$7.4 \pm 2.1$	$1.92 \pm 0.29$	$2.50 \pm 0.27$	$5.39 \pm 0.32$	$1.67 \pm 0.24$	$0.67 \pm 0.26$	$36.4 \pm 1.6$	$14.70 \pm 0.73$	...	...
042	$12 \pm 12$	$< 1.7$	$2.2 \pm 1.4$	$4.1 \pm 1.4$	$5.4 \pm 1.4$	$< 3$	$16.7 \pm 3.2$	$2.1 \pm 2.0$	$8.1 \pm 2.4$	$4.6 \pm 2.3$
043	$< 0.79$	$< 0.34$	$0.32 \pm 0.26$	$0.39 \pm 0.18$	$0.53 \pm 0.19$	$< 0.21$	$4.42 \pm 0.32$	$2.25 \pm 0.22$	$0.62 \pm 0.21$	$0.60 \pm 0.22$
048	$< 4.5$	$1.64 \pm 0.88$	$< 1.7$	$< 0.83$	$< 1.2$	$< 1.4$	$3.97 \pm 0.60$	$< 1.2$	$< 1.6$	...
050	$4.7 \pm 1.9$	$0.70 \pm 0.26$	$0.27 \pm 0.20$	$0.44 \pm 0.15$	$0.98 \pm 0.17$	$0.29 \pm 0.18$	$3.26 \pm 0.28$	$3.41 \pm 0.27$	$1.04 \pm 0.21$	$0.85 \pm 0.22$
051	$7.1 \pm 2.4$	$1.42 \pm 0.28$	$1.63 \pm 0.24$	$3.55 \pm 0.24$	$3.92 \pm 0.26$	$0.61 \pm 0.18$	$25.7 \pm 1.1$	$10.92 \pm 0.52$	$4.23 \pm 0.28$	$3.59 \pm 0.27$

Note. — Table 7 is published in its entirety in the electronic edition of the *Astrophysical Journal*. A portion is shown here for guidance regarding its form and content.

<sup>a</sup>Nuclear rest-frame emission-line equivalent widths in Angstroms, corrected for underlying stellar absorption as described in § 3.3. We give  $1\sigma$  upper limits assuming two significant figures and identify them using a  $<$  sign. The errors only include statistical measurement uncertainties. We do not give equivalent widths for the following objects because their nuclear spectra cannot be modeled reliably using the algorithm described in § 3: NGC 1068 (054), NGC 1275 (070), NGC 3998 (214), NGC 4051 (223), and MRK 0315 (382).